Detection of Energetic Neutral Atoms

Peter Wurz

Group for Space Research and Planetary Sciences
Physikalisches Institut, Sidlerstrasse 5, Universität Bern, CH-3012 Bern, Switzerland

Camera-ready Copy for

The Outer Heliosphere: Beyond the Planets

Manuscript-No. –, edt. K. Scherer, H. Fichtner, E. Marsch, Copernicus Gesellschaft e.V.,
Katlenburg-Lindau, Germany, 2000, pages 251–288.

Offset requests to:
Peter Wurz
Universität Bern, Physikalisches Institut
Sidlerstrasse 5, CH-3012 Bern
Switzerland

Book: The Outer Heliosphere: Beyond the Planets
MS No.: –, edt. K. Scherer, H. Fichtner, E. Marsch, Copernicus Gesellschaft e.V., Katlenburg-Lindau, Germany, 2000, pages 251–288.
First author: Wurz

Detection of Energetic Neutral Atoms

Peter Wurz

Group for Space Research and Planetary Sciences
Physikalisches Institut, Sidlerstrasse 5, Universität Bern, CH-3012 Bern, Switzerland

1 Resume

The techniques for the detection of energetic neutral atoms (ENAs) currently in use and those developed for future application in space research are reviewed. Various sources of ENA are currently the target of intense investigations. Typically, ENAs are produced from plasma ions by charge-exchange with a neutral background gas. In addition, the neutral interstellar gas penetrating the heliosphere is also an important source of ENAs. Since ENAs travel virtually unperturbed for very long distances they can be used for remote sensing of space plasma populations, for objects ranging from planetary magnetospheres at all scales to the quite distant heliospheric termination shock. The ENA sources and their respective energy ranges and fluxes are discussed briefly. The energy range of ENAs accessible to direct observation spans from about 10 eV to more than 1 MeV. On the high-energy side, the energy limit for ENAs is given by experimental limitations, but there are also good scientific reasons why ENA fluxes should be negligible at these energies. At the low-energy side, the limit is given by the available instrumentation. Several fundamentally different experimental techniques are necessary to cover such a large energy range. Moreover, not just the mere detection of the ENAs is desired but also the measurement of their arrival direction, possibly in two dimensions, is needed for many applications.

2 Introduction

Energetic neutral atoms originate from locations in space where an energized plasma and a cold neutral background gas co-exist. When encountering a neutral gas atom, singly charged plasma ions can undergo a charge-exchange process resulting in an energetic neutral atom (ENA) and a low-energy ion. Being electrically neutral, the newly created ENA will leave the plasma along a ballistic trajectory, carrying with it its initial energy from being an ion of the plasma population. Macroscopically, these events occur at random, and ENAs exit the plasma population in all directions. A typical source of ENAs are planetary magnetospheres, where ions undergo charge-exchange processes with the exospheric neutral gas. The exception to this creation scenario is the flux of interstellar gas, where neutral particles from the local interstellar medium penetrate the heliosphere with considerable velocity, which classifies them as ENAs as well. Unlike charged particles, ENAs can travel large distances through space with minimal disturbances. By recording ENA fluxes as a function of the observational direction, one can construct two-dimensional images of a plasma population. Global images of a space plasma population will help to answer questions that could not be addressed by statistical analysis of 40 years of *in situ* measurements, which have the difficulty to distinguish between spatial variations and temporal changes.

A very thorough account of ENA instrumentation was given recently by Gruntman (1997) and will not be reproduced here. ENA instrumentation for particle energies $>$ 10 keV has also been reviewed by McEntire and Mitchell (1989) and more recently by Hsieh and Curtis (1998). The latter paper also contains a detailed history of ENA instrumentation and scientific accomplishments.

The investigation of space plasmas utilizing emitted ENAs began with the discovery of energetic hydrogen atoms in the aurorae in 1950 (Meinel, 1951). Since then, ENA emission from the Earth's magnetosphere has been observed on several occasions. Furthermore, the emission of energetic neutral particles has been observed from the magnetospheres of Jupiter and Saturn (Kirsch et al., 1981a,b). However, it was not until 1987 that the first ENA image of a magnetic storm was constructed from measurements recorded with the ion detectors on the IMP 7/8 and ISEE spacecraft (Roelof, 1987). In all the above cases ENAs were measured by instruments designed for energetic ion detection, during periods when the ambient energetic ion fluxes were low and ENA fluxes could dominate the instrument response.

In 1990 the first dedicated ENA instrument, the INCA instrument (Mitchell et al., 1993), was selected for the *Cassini* mission to study Saturn's magnetosphere. *Cassini* was launched on October 15, 1997, and will arrive at Saturn in 2002. In 1997 the IMAGE mission was selected by NASA (Burch, 1995). The IMAGE mission is a Medium-size Explorer mission (MIDEX) and has three ENA imaging instruments covering the energy range from 10 eV up to several MeV. IMAGE is scheduled for launch early in 2000. Development of ENA instrumentation has intensified dramatically since 1990. ENA imaging is now a rapidly expanding field of research because the required experimental techniques have matured resulting in many opportunities for application.

2.1 Charge Exchange

Charge exchange of singly-ionized plasma ions to produce energetic neutral atoms is fundamental to many ENA sources. The corresponding neutral gases are the geocorona for the Earth's magnetosphere, a planetary exosphere for a planetary magnetosphere, the penetrating interstellar medium inside the heliosphere, and the local interstellar medium in the boundary region of the heliosphere (at the termination

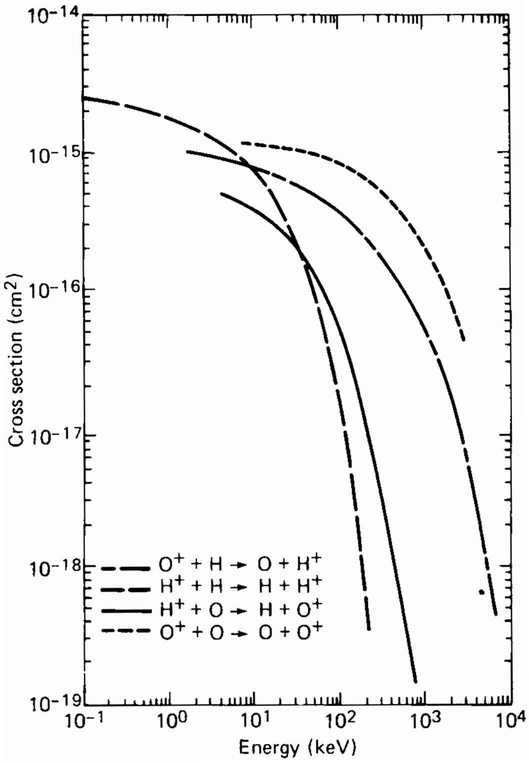

Fig. 1: Charge-exchange cross sections of energetic H^+ and O^+ ions as a function of total ion energy for electron pickup from cold neutral hydrogen and oxygen (figure is taken from a compilation by McEntire and Mitchell, 1989).

shock and the heliopause).

The probability that a given charge exchange process will actually take place in a collision is expressed as a reaction cross section. The charge-exchange cross sections for singly charged hydrogen and oxygen ions with cold neutral gas are shown in Fig. 1. At low ion energies the cross sections for charge exchange (electron pickup) are in the range of 10^{-15} cm^2, which is a rather high value. The H^+ cross section begins to decrease strongly for proton energies above 10 keV, and drops dramatically above 50 keV. This is a very important constraint on ENA production, and it assures that ENA hydrogen spectra will be concentrated below $\approx$ 200 keV. Quite general, the electron pickup cross section is a strong function of the ion velocity. Thus, the O^+ cross section begins to decrease strongly around 200 keV, and drops dramatically above 1 MeV. This behavior is quite general for all elements (see compilation by Spjeldvik and Rothwell, 1985). At higher energies the energy spectra of plasma particles typically fall off toward increasing energies. Since the cross sections for charge exchange drop also with increasing energy, the energy spectra of ENAs are very steep at higher energies, with a cut-off around 1 MeV.

ENA production is a function of ion energy and species, and of the density and composition of the neutral gas. The ENA unidirectional flux for species i is given by the line-of-sight integration

$$f_i(E) = \sum_k \sigma_{ik}(E) \int j_i(E,l) n_k(l) dl \qquad (1)$$

where $n_k(l)$ is the density of the component k of the neutral gas, $j_i(E,l)$ is the directional singly charged ion flux along the line-of-sight at each point l for species i within the source volume, and $\sigma_{ik}(E)$ is the charge-exchange cross section for the involved species. The sum extends over all constituents of the neutral gas contributing to the charge exchange.

For ions heavier than protons, several potential charge states are available. For helium, for example, one must also consider the competing process of doubly ionizing a singly charged helium ion in the cold neutral gas. The cross section for this process initially increases with energy, and starts to have an appreciable cross section of a few 10^{-17} cm^2 at energies of 100 keV for helium; for oxygen this energy is even lower, around 10 keV and with cross sections exceeding 10^{-16} cm^2 (Spjeldvik and Rothwell, 1985). Highly energetic particles, with energies exceeding MeVs, can travel even in the dilute interstellar medium only $\approx 10^4$ AU[†] before they are all ionized.

2.2 Sources of Energetic Neutral Atoms

Various sources of energetic neutral atoms exist in space. These have been reviewed in detail by Gruntman (1997), and will be discussed here only briefly. Figure 2 gives an overview of the different sources of energetic neutral particles that can be observed in space, together with their approximate energy range. The energy range of ENAs is divided into three sub-ranges: low-energy neutral atoms (LENA), medium-energy neutral atoms (MENA), and high-energy neutral atoms (HENA). This division originates from the different experimental techniques necessary in these energy ranges rather than from the different physical natures of these ENAs. Note that there are other classifications of these energy ranges in the literature depending on the preference of the authors. No single particle analyzer can cover the entire energy interval from about 10 eV to beyond 1 MeV. In this paper we consider atoms to be energetic neutral atoms if they have kinetic energies clearly higher than can be reached by thermodynamic processes typical for planetary atmospheres (roughly speaking, energies exceeding 1 eV). This classification is somewhat arbitrary and is driven by the lowest energy ENA which can be recorded by current instrumentation. The high end of the ENA energy range is given by limitations imposed by the measurement techniques as well as by scientific reasons (see below).

2.2.1 Magnetospheric Particles

Magnetospheres are vast regions around planets filled with magnetic fields, electric fields, matter, and energy, and are formed by the solar wind plasma flow around planets with an intrinsic magnetic field. The planetary magnetic field presents an

[†] 1 AU = 1 astronomical unit = the distance from Sun to Earth; 1 AU = $1.4960 \cdot 10^{11}$ m.

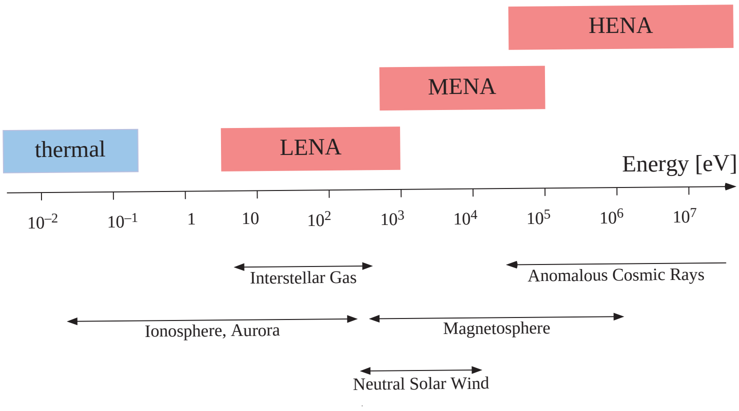

Fig. 2: Energy range of ENAs and their classification into low-energy neutral atoms (LENA), medium-energy neutral atoms (MENA), and high-energy neutral atoms (HENA). Possible sources of ENAs and their approximate energy range are indicated.

obstacle for the solar wind, and a bow shock is formed in front of the planet. The size and the shape of the magnetosphere are determined by the strength and orientation of the magnetic field with respect to the solar wind flow. Magnetospheres are usually compressed at the sunward side and elongated at the anti-sunward size (the magnetospheric tail). The magnetosphere is highly structured, with different plasma populations which are fed by the solar wind on the outer boundary and by the ionosphere from inside (Banks, 1979). For ENA production near Earth, in particular in the HENA range, the ring current and the inner radiation belt are of greatest importance. The Earth's radiation belt region contains electrons (outer Van Allen belt) and ions (inner Van Allen belt) such as protons, helium, carbon, oxygen, and other ions with energies from less than 1 keV to hundreds of MeV (Spjeldvik and Rothwell, 1985). Particles below 200 keV are the main contributors to the energy density of the ring current particle population. ENA fluxes from these regions have been estimated to be in the range 0.1 – $10^3/(\mathrm{cm}^2$ s sr keV) for energies $\geq$ 20 keV, varying strongly with geomagnetic activity (McEntire and Mitchell, 1989). Detection of HENAs from the Earth's ring current has been shown with measurements from the IMP 7/8 and ISEE-1 satellites (Roelof et al., 1985; Roelof, 1987). From a simple model calculation one derives ENA fluxes from the Earth's ring current of 16 H atoms$/(\mathrm{cm}^2$ s) between 10 and 100 keV, and 3 O atoms$/(\mathrm{cm}^2$ s) between 60 and 200 keV (Hsieh and Curtis, 1989). The most recent observation gave an upper limit of 7 particles$/(\mathrm{cm}^2$ sr s) in the energy interval from 77 to 200 keV (Wilken et al., 1997). Actually, it has long been recognized that the charge exchange between the energetic ions and the exospheric and geocoronal hydrogen atoms is an effective means to dissipate the energy in the ring current during a magnetic storm. The polar cusp regions, where the ionosphere and the magnetosphere couple, is the source of ENAs mostly in the LENA range.

2.2.2 Interstellar Gas

The solar system is immersed in a large gas cloud of low density, the so-called local interstellar medium (LISM). The interaction between the Sun and the LISM manifests itself in the buildup of the heliosphere. The Sun is the source of the highly supersonic flow of plasma (mostly protons and electrons) called the solar wind, which flows away from the Sun with velocities of 300–800 km/s (e.g., see Yermolaev, 1991). The dynamic pressure of the expanding solar wind flow decreases with distance from the Sun and the solar wind comes to rest at a certain point. The cavity in the LISM containing the solar wind is called the heliosphere. Estimates of the size of the heliosphere vary between 100 and 150 AU at the upwind side. The heliospheric cavity is shielded from the inflow of ions from the LISM, since the solar wind plasma is highly magnetized compared to the interstellar medium[†]. Only the neutral particles can enter the heliosphere. However, some of these neutral particles are ionized by the solar UV radiation and swept away from the Sun by the solar wind (Möbius et al., 1985). These ions are called pick-up ions (see review by Mall, this volume, and references therein). Because of the relative motion of the solar system with respect to the local interstellar medium, some of the neutral particles of the LISM deeply penetrate into the solar system as far as the region of the inner planets. In the vicinity of the solar system the particles of the local interstellar medium are mostly individual neutral atoms. These neutral atoms, which originate outside the solar system and are quite energetic due to their relative velocity, are subject to direct analysis.

The physical parameters of the local interstellar medium have recently been reviewed by Geiss and Witte (1996). The flow of the interstellar gas inside the heliosphere, as determined from the interstellar helium atoms (Witte et al., 1996), is in the direction L_∞ = 73.9±0.8° and B_∞ = –5.6±0.4° in ecliptic coordinates with a velocity of 25.3±0.4 km/s. The temperature of the interstellar helium is T_∞ = 7000±600 K. This flow velocity corresponds to a specific energy of $E/m \approx$ 6.6 eV/nuc for an observer at rest in the solar system. The interstellar gas consists mainly of neutral hydrogen and helium atoms, with the hydrogen density being 11.5±2.5·10^{-2} cm^{-3} and the helium density being (1.4 – 1.7)·10^{-2} cm^{-3} (H/He = 7.7±1.3). Heavier elements, like oxygen, nitrogen, neon, and carbon, have an atomic abundance in the range between some 10^{-4} to 10^{-6} with respect to hydrogen (Geiss and Witte, 1996). At the Earth's orbit there is a considerable loss in the interstellar atom flux due to photo-ionization by the Sun, in particular when the interstellar atoms have to move past the Sun to arrive at the observer. For an observer on Earth orbit, the interstellar helium flux is in the range of (2 – 12)·$10^4/(cm^2$ s) depending on the season, with a strong enhancement for a few days to 3.3·$10^5/(cm^2$ s) due to gravitational focusing (mid December). The highest fluxes are obtained early in the year when the Earth is approaching the upwind direction (June 15 each year). The highest fluxes of interstellar hydrogen on Earth orbit are $10^4/(cm^2$ s) close to the upwind direction. In the downwind direction interstellar hydrogen is completely ionized.

[†]The effectiveness of the shielding decreases at high particle energies and vanishes beyond ≈ 15 GeV.

The measurement of the physical parameters and the composition of the interstellar gas that penetrates into the heliosphere will provide information on the interaction of the expanding solar atmosphere (the heliosphere) with the local interstellar cloud. Different species of the interstellar gas will have different velocities and temperatures inside the heliosphere as a result of this interaction. Once this interaction is understood, the chemical and isotopic compositions of the local interstellar medium can be inferred. This information might also provide important data on the synthesis of light nuclei in the early universe (the Big Bang) and the continuing processes of nucleosynthesis and galactic evolution.

2.2.3 Neutral Solar Wind

The neutral solar wind is believed to originate from charge exchange between solar wind ions and the interplanetary neutral gas (see summary by Gruntman, 1997). An experiment to measure the neutral solar wind was prepared in the early 1980s, but was not flown yet (Gruntman et al., 1989). The neutral solar wind atoms move in the anti-sunward direction with approximately the solar wind velocity. The neutral solar wind consists of hydrogen and helium atoms. Heavier solar wind ions are more difficult to neutralize due to their higher charge state in the solar wind. Depending on the observer position at the Earth's orbit, the estimated flux is 10^3 – $10^4/(\mathrm{cm}^2\ \mathrm{s})$, which constitutes a 10^{-5} – 10^{-4} fraction of the solar wind flux (Gruntman, 1997). Further out in the heliosphere this flux might increase to 10% – 20% and play an important role in the shaping of the global heliosphere. The neutral solar wind is not contained within the heliosphere. It escapes into the local interstellar gas, and the resulting perturbation of the local interstellar medium is possibly much larger than the extent of the heliosphere.

2.2.4 High-Energy Heliospheric Neutral Atoms

The ENAs of the high-energy heliospheric neutral atom class also start as singly charged positive ions, before picking up an electron from a neutral atom of the ambient gas (Hilchenbach et al., 1998, this volume). The shape of the energy spectrum of these ENAs is derived from the original ion spectrum convolved with the sum of the charge-exchange cross-sections, weighted by the number densities of the respective neutral atoms in the ambient gas. Since the ion fluxes of most varieties of space plasmas decrease with increasing ion energies, as do the cross-sections above 10 keV/nuc, the fluxes of high-energy heliospheric neutral atoms decrease even more with increasing energy resulting in steeper energy spectra. The singly charged positive ions of the low-energy anomalous cosmic rays (ACR) protons have been identified to be the main source for the heliospheric neutral hydrogen atoms (Hilchenbach et al., 1998). The ambient gas for facilitating the charge-exchange reaction originates from the local interstellar medium surrounding the heliosphere, from which the neutral atoms penetrate into the heliosphere (see Chapter 2.2.2). The intensity of the ENA flux of high-energy heliospheric neutral atoms is derived from the line-of-sight column integral over the space where the ion population overlaps the ambient gas. Since the neutral atoms from the interstellar medium fill almost the whole heliosphere, with the exception of the small volume in the vicinity of the Sun (a volume of a few AU radius), the location of "birth" of the high-energy heliospheric neutral atoms is somewhere in the heliosphere and perhaps even beyond the termination shock.

Although not a dedicated ENA instrument, the HSTOF sensor of the CELIAS instrument on the SOHO spacecraft was able to detect energetic hydrogen atoms of heliospheric origin (Hilchenbach et al., 1998). The differential flux in the energy range from 55 keV to 80 keV was found to be very low, approximately $10^{-4}/(\mathrm{cm}^2$ s sr keV). A strong increase of the flux by a factor of about three was observed in the anti-apex direction of the flow direction of the interstellar gas with respect to the solar system. The INCA instrument (Mitchell et al., 1996), a dedicated ENA instrument on the *Cassini* mission to Saturn, promises to provide even better data since it has a larger geometrical factor and a lower energy threshold than HSTOF.

2.3 Principal Functions of an ENA Instrument

The principal functions an ENA instrument has to perform are ENA detection and background suppression. Background arises from charged particles, from penetrating high-energy particles, and from UV and EUV photons. Usually, these background sources are far more intense than the ENA flux.

2.3.1 Rejection of Charged Particles

The source regions releasing ENAs are of course also populated with energetic charged particles, which by far outnumber the ENAs. Furthermore, for most missions on which ENA instruments are flown there will be significant local charged-particle fluxes at the location of the spacecraft. For magnetospheric missions one has to assume that the local energetic charged-particle fluxes will be orders of magnitude larger than the ENA flux to be measured. For most particle detectors, the detection of charged particles is similar, if not identical, to the detection of a neutral atom of the same energy. Thus, charged particles cannot be distinguished from energetic neutral particles at the detector. Therefore, these charged particles have to be prevented from entering the ENA instrument.

Charged particles up to some energy can be hindered from reaching the detector by deflecting them out of the path of the ENAs in the entrance system of the instrument and absorbing them somewhere in the structure. This can be accomplished either with electric or magnetic fields, or both. Electric fields are used in almost all cases for charged-particle rejection. The first segment of an ENA instrument is usually a mechanical collimator, which defines the overall field-of-view of the instrument. This collimator can be built such that it consists of two closely spaced metallic plates. If these plates are supplied with high voltages of alternate polarity, a capacitor for charged-particle deflection is realized. Ignoring fringe fields, charged particles with an energy-per-charge below

$$E/q = \frac{1}{4} U \left(\frac{L_E}{2D} \right)^2 \tag{2}$$

will be deflected into the collimator structure with deflection plates of a length L_E and a separation D if a voltage U is applied between the plates. For a typical voltage U = 10 kV and the geometrical dimensions L_E = 0.12 m and D = 0.004 m, the propagation of ions and electrons below $E/q \approx$ 570 kV beyond the deflection plates is prevented. By optimizing the geometrical parameters of the charged-particle rejection system and increasing the voltage between the plates, suppression of ions and electrons up to several MeV is feasible. Beyond that energy, charged particles cannot be separated from the ENAs, and the unambiguous detection of ENAs is not possible anymore. The charged-particle rejection presently limits the energy range for which ENA measurements are possible to several MeV.

Particles impinging on solid surfaces will release secondary electrons. These secondary electrons also have to be prevented from passing further into the instrument. This can be done by applying a magnetic field perpendicular to the electric field established by the charged-particle rejection plates. Usually, permanent magnets are used for this purpose, which have the advantage of zero power consumption. With a magnetic field strength B, particles with mass m and energy-per-charge below

$$E/q = \frac{qB^2}{2m}\left(\frac{D^2 + L_M^2}{2D}\right)^2 \tag{3}$$

will be deflected into the collimator structure. With a length L_M = 0.02 m of the magnet and a plate separation D = 0.004 m we find that electrons below $E \approx$ 24 keV are kept from moving beyond the entrance system for a magnetic field B = 0.01 T. Using larger magnets and higher field strengths, charged particles of higher energies can be prevented from entering the instrument. However, this usually requires a yoke and a magnetic shield, which may be unacceptably heavy.

Charged-particle rejection collimators with a number of different geometries have been proposed and built. One simple and effective configuration consists of a stack of parallel metal plates of length L and separation D, with L/D chosen to define the field-of-view of the instrument. The applied voltage between two adjacent plates defines the maximum energy-per-charge of the particles, which can be rejected according to eq. 2. However, it is not enough to deflect incoming ions to hit a plate in the collimating system, since these particles might be scattered off the surface and continue as neutral particles further into the instrument to create a background signal. Thus, with a dedicated mechanical design of these plates, one has to ensure that particles hitting a plate cannot be reflected toward the detector. Roughening of the plates or serrations are appropriate means to reduce the background arising from particles scattered in the collimating system. If high suppression factors are needed ($\approx 10^3$ and more), such a charged particle deflection system should always be tested for its effectiveness in suppressing unwanted flux at the detector. Experience shows that the amount of scattered particles contributing to the recorded signal is difficult to assess theoretically and may differ by orders of magnitude from the laboratory results (Keath et al., 1989).

2.3.2 Rejection of Penetrating Particles

Particles with very high energy (exceeding 1 MeV/nuc) can penetrate the thin walls of space instrumentation and can cause background signals when hitting a detector.

Near a planet, particles with very high energies originate mostly from the radiation belts. At locations near the Earth, fluxes of electrons geomagnetically trapped in the radiation belts are in the energy range of 3 – 5 MeV, and their fluxes are typically in the range from 10^2 to $10^5/(\mathrm{cm}^2\ \mathrm{s})$. The proton fluxes at energies above 100 MeV can be greater than $10^4/(\mathrm{cm}^2\ \mathrm{s\ sr})$ (see, e.g., McEntire and Mitchell, 1989). An appropriate choice of orbit as well as passive shielding of the instrument can reduce the background due to energetic particles from radiation belts to a manageable level.

Another source of highly energetic particles is cosmic rays, which consist of approximately 83% protons, 13% alpha particles, 1% heavier nuclei, and 3% electrons. This composition extends over an energy range from a few 100 MeV to $> 10^{20}$ eV (Smart and Shea, 1985). There are no local planetary sources for these high energy ions, but the electron component below about 20 MeV is dominated by Jovian electrons. In the ecliptic plane the intensity of cosmic ray particles is dependent on the solar cycle, with the modulation being inverse to the solar activity. The isotropic flux of galactic cosmic rays at 1 AU at sunspot minimum is 4 $\mathrm{protons}/(\mathrm{cm}^2\ \mathrm{s})$ and at sunspot maximum it is 2 $\mathrm{protons}/(\mathrm{cm}^2\ \mathrm{s})$. In the energy range between 1 MeV/nuc and $\leq$ 70 MeV/nuc there are, in addition to the galactic cosmic rays, the anomalous cosmic rays (ACR), which are quite variable. ACRs are thought to be pickup ions accelerated at the heliospheric termination shock. Transient solar events (e.g., flares, solar particle events, coronal mass ejections) can also be sources of highly energetic particles in the energy range up to approximately 100 MeV, with considerable fluxes for days.

These cosmic ray particles are so energetic that they cannot be effectively shielded in an instrument on a spacecraft, since the necessary mass would be prohibitive. For a simple single-detector ENA instrument the background from highly energetic particles can be reduced by an active anti-coincidence shielding around the detector. More complex instruments using two or more detectors for a multi-parameter measurement of the ENA event will substantially reduce the background from highly energetic particles by the requirement of coincidence and by further electronic signal processing.

2.3.3 Photon Suppression

Ultraviolet (UV) photons and extreme UV photons (EUV)[†] can cause unacceptable background count rates in sensitive detectors, either when a UV or EUV photon falls directly onto the detector, or via the release of photoelectrons somewhere inside the instrument, which then make their way from the location of photoelectron release to the detector. Unfortunately, the source regions of UV and EUV photons are most of the time the same regions from which ENAs escape.

[†] EUV radiation usually refers to photons which are in the wavelength range below the *H* Lyman α line.

UV photon fluxes, usually dominated by the H Lyman α line at 121.57 nm (10.2 eV), can be quite high in many locations accessible for current spacecraft. The solar H Lyman α flux is about $4{\cdot}10^{11}$ photons/(cm^2 s) at 1 AU (Stix, 1991) and depends on the phase in the solar cycle. The solar H Lyman α flux is as much as the photon flux in the whole solar spectrum below 150 nm besides the H Lyman α line. However, the integrated UV flux up to 250 nm is more than 200 times the solar H Lyman α. This number is important when evaluating background due to photoelectron emission, since most metals have a work function around 5 eV (Hölzl and Schulte, 1979).

The solar H Lyman α radiation is resonantly scattered by neutral hydrogen atoms of the Earth's exosphere to create a widespread H Lyman α emission. At a distance of several R_E from the Earth this UV flux has intensities ranging from 500 Rayleigh[‡] to 10^4 Rayleigh ($5{\cdot}10^7$ to 10^9 photons/(cm^2 s sr)) depending on the look direction and the distance from Earth (Rairden et al., 1983, 1986).

The solar H Lyman α radiation is also resonantly scattered by neutral hydrogen atoms of interstellar origin penetrating the heliosphere. This H Lyman α radiation originates from the whole sky, but it shows an asymmetry with respect to the flow direction of the interstellar gas. The upwind intensity of this H Lyman α glow is 600 – 800 Rayleigh, and the downwind intensity is 200 – 400 Rayleigh (Frisch and York, 1986). Just for completeness, one can also observe the He I glow from solar photons at 58.4 nm scattered by neutral interstellar helium with a downwind intensity of about 12 Rayleigh.

Usually, an ENA instrument must attenuate the incident photon fluxes to acceptable levels or separate the incident photons from the incident particles. Depending on the type of instrument, there are various ways in which the UV suppression can be accomplished. Again, using a multi-parameter measurement for ENA registration will also reduce the background arising from UV photons substantially.

2.3.4 ENA Detection

The capability to detect ENAs with good mass, energy, and directional resolution constitutes the basis of ENA imaging. Imaging is necessary for almost all applications involving the detection of ENAs. If only one species, for example hydrogen, is expected to dominate the measured ENA flux, then a single measurement of the energy would suffice. However, in most cases one is interested in the elemental and perhaps even in the isotopic composition of the ENA flux, which results in demands of sufficient mass resolution and high dynamic range of these instruments. Typically, an ENA instrument has to provide a dynamic range to cover ENA fluxes from 10^{-3} to 10^5/(cm^2 s sr). Depending on the variability of the object, time resolutions from minutes in magnetospheric research (substorm onset) to days (ring current decay) to months for the penetrating interstellar medium have to be handled by ENA instrumentation. The challenge to remote sensing via ENAs lies in combining mass spectrometry with imaging within the stringent limitations imposed by an application on a spacecraft.

[‡] 1 Rayleigh = $10^6/4\pi$ photons/(cm^2 s sr)

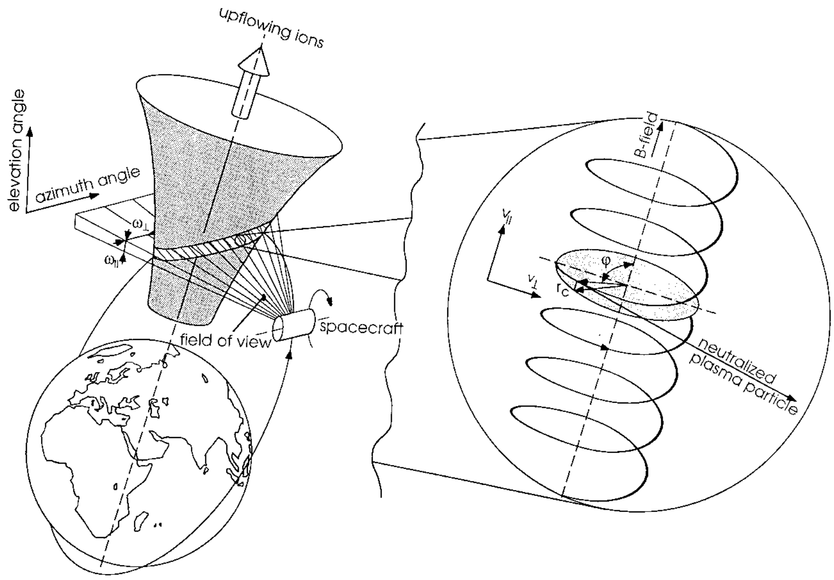

Fig. 3: Schematics of the recording of 2D ENA images by remote sensing of a plasma volume using a 1-D imaging instrument and the spacecraft rotation, as used by the LENA instrument on the IMAGE mission. The IMAGE spacecraft will be placed in an elliptical orbit of 500 km by 7 R_E at an inclination of 90°. Ten sectors will be used for angular mapping in the azimuth direction, the rotation of the satellite for mapping in the elevation angle (from Wurz et al., 1995).

We can distinguish between two-dimensional imaging instruments, one-dimensional imaging instruments, and non-imaging telescopes. Two-dimensional imaging is typically performed from a three-axis stabilized spacecraft with an ENA imager recording the arrival direction of a particle in two dimensions while starring at the object of interest with a sufficiently large field-of-view to cover the entire object. In one-dimensional imaging, the ENA imager records the arrival direction of the particle only in one direction, with the other direction being narrowly collimated in such an instrument. The other dimension of the image is obtained by scanning over the object using the rotation of the spacecraft. The one-dimensional imaging scheme is illustrated in Fig. 3. Telescopes have no intrinsic imaging capability, but of course a defined field-of-view. To obtain a two-dimensional image with a telescope one uses the spin of the spacecraft for one direction, and a scanning platform, which points the telescope in the desired direction, for the other direction. A one-dimensional imager on a spinning spacecraft has become a favorite configuration for ENA instruments. On the IMAGE mission three such instruments are used for LENA, MENA, and HENA detection (Burch, 1995).

The recorded ENA image is a line-of-sight integral through the whole plasma volume (Wurz et al., 1995; Hsieh and Curtis, 1998). The interpretation of such images includes forward modeling of the observed plasma volume and comparison with the recorded data. The modeling also has to include the density distribution of the neutral gas for the charge exchange, which can be quite variable with time (e.g., the Earth's exosphere). Since the image resolution is often limited in current ENA imagers, the instrument function also has to be considered in the forward modeling. The modeling of the initial plasma population is an iterative process until satisfactory agreement between the model and the measured data is obtained. A comprehensive description of the modeling techniques required for remote imaging with ENAs is given by Roelof (1987).

3 The Foil Collection Technique

The foil collection technique is based on the penetration and capture of energetic particles in solid matter. Appreciable trapping efficiencies are found for particles with energies above approximately 50 eV. The collection medium is usually a foil to facilitate handling in space and in the laboratory on ground. Moreover, using thin foils rather than more massive collection geometries has the advantage that the background from particles initially contained in the medium is considerably lower. In space, these foils are exposed to the flux of energetic particles of interest for a certain time (ranging from days to years). After exposure, the foils are brought back to the Earth for analysis of the entrapped material. In the laboratory the collected particles are released by heating samples cut which are cut from the exposed foils. The released gases are then analyzed in a mass spectrometer. In the analysis of these particles, not only can the amounts of the various noble gas isotopes be measured, but additional information can be obtained by heating the returned collector foils in increments. At the lowest temperatures the least tightly bound particles are released. These are the ones trapped closer to the surface, because their energy when hitting the foil was the lowest. By increasing the temperature in steps, more and more particles will be set free from deeper inside the collection foil until all entrapped material is released. This is shown in Fig. 4 where, for certain temperature steps, the dependence of the fraction of released gas on the initial energy of the trapped particle can be seen clearly. Since the collected particle sample is extremely small, special mass spetrometric techniques are required for the measurement. The foil collection technique is particularly well suited for the analysis of noble gases for two reasons. One reason is that the foils originally contain very small amounts of noble gases. The second reason is that the background of noble gases in laboratory mass spectrometers can be kept very low. Background from other gases can be effectively removed by, e.g., the use of a chemical getter, which removes everything but noble gases.

The technique of using foils to entrap energetic particles in space for later analysis in the laboratory by mass spectrometric means was first developed for the Apollo missions to the Moon by the University of Bern. In this application, noble gas elemental and isotopic composition of He, Ne, and Ar in the solar wind was measured (Geiss et al., 1970, 1972). Later, on the Skylab missions, this technique was used to analyze the isotopes of precipitating magnetospheric particles (Lind et al., 1979). This same technique has also been used on two sounding rockets to investigate auroral particles (Axford et al., 1972; Bühler et al., 1976). In principle, every piece of equipment which has been out in space and has been exposed to energetic par-

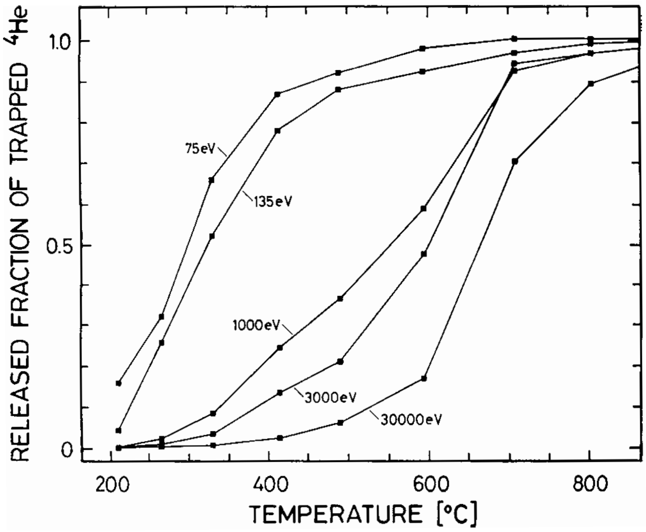

Fig. 4: ^{4}He released from copper-beryllium collection foils by stepwise heating. The symbols indicate the fraction of gas released at the individual heating steps. Several different energies to entrap ions have been used, as indicated (from Bühler et al., 1993).

ticles will contain trapped particles. For example, the astronauts from the Apollo 12 mission returned several pieces of the Surveyor 3 spacecraft (unmanned), which had landed on the Moon in 1967. Analysis of such a piece yielded results for the He and Ne abundance and isotopic composition in the solar wind (Bühler et al., 1971) similar to those obtained from the analysis of the dedicated foils (Geiss et al., 1970). However, for most pieces having been in space the exposure history is not well known or not well defined, and meaningful interpretation of the released gases is not possible.

The first application of the foil collection technique to energetic neutral atoms was the Interstellar Gas Experiment (IGE) on the Long Duration Exposure Facility (LDEF) mission (Lind et al., 1991; Bühler et al., 1993). The purpose of the IGE instrument was to detect and, if possible, to isotopically analyze the noble gas component of the local interstellar medium. The LDEF satellite was in a low-Earth orbit from April 1984 until January 1990. In the IGE instrument beryllium-copper collector foils (2% beryllium by weight) of 15 μm thickness were used for the collection of interstellar gas atoms. On the surface of these foils a thin beryllium oxide had been formed. Six foils mounted on separate plates were placed at the bottom of a box-like collector unit; five of these foils could be moved in and out of the ENA flux. The design of the collector unit is shown in Fig. 5. The open end of the box-like collector established the field-of-view of the collector for particles to reach the foil.

Seven of these collectors were mounted on the LDEF spacecraft with different viewing directions (shown in Fig. 6). One axis of LDEF pointed radially outward from the Earth and one axis pointed forward along the velocity vector. The center

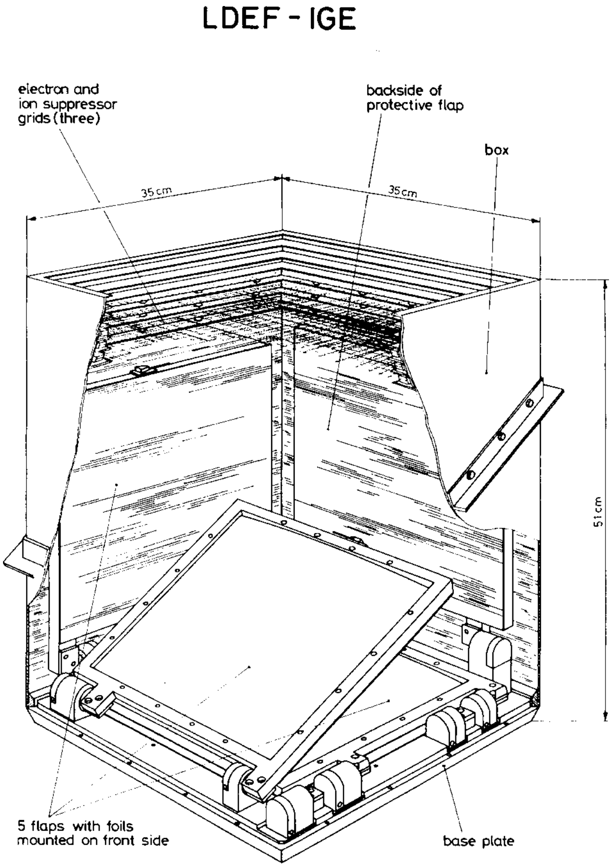

Fig. 5: One of the seven collectors of the IGE instrument on LDEF. The collector contains a cassette with six plates (five plates are moveable, one plate is fixed) holding one foil each. The third plate is shown turned up somewhat to allow a view of the fourth foil (from Lind et al., 1991).

line of every collector, standing orthogonally on the center of the foil, defined the orientation of the field-of-view relative to the LDEF orientation and, ultimately, to the celestial sphere. The collectors were oriented so as to optimize the collection of interstellar particles and to reduce the collection of particles from other sources. Since the orbital velocity of LDEF was sufficiently high, atmospheric atoms would have had enough energy that a small percentage could possibly be rammed into the foils as a background, but the orientation of the collectors prevented that. In addition, a series of knife-edge baffles near the opening of the collectors and serrations along the inner walls of the collectors prevented atmospheric particles from striking the walls and reaching the foils in a single bounce. An additional source of background particles is the flux of charged particles, which was suppressed by a high-voltage grid at +1250 V mounted across the entrance of the collectors. In the case of the LDEF mission, these ions originated from the magnetosphere, particularly from double charge-exchange reactions (Moritz, 1972; Tinsley, 1981; Voss et al., 1993). During flight, however, the electrical system of IGE had a malfunction and only one of the six foils of each collector unit got exposed. The high voltage for the suppression of charged particles failed as well. Therefore, this resulted in

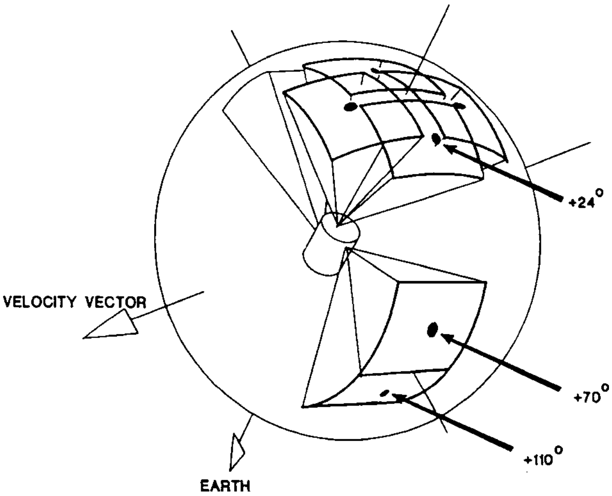

Fig. 6: The orientation of the fields-of-view of the seven collectors of the IGE instrument relative to the LDEF satellite.

a severe contamination of the exposed foils with magnetospheric particles. Intense photon fluxes do not pose a problem for the foil collection technique.

The advantages of the foil collection technique are the simple instrumentation and the simple operations in space. Large collection areas and high collection efficiencies are achieved with this technique. In addition, analysis of material in laboratories on Earth can be done with much better sensitivity and resolution than is possible on a space-borne instrument. For example, the direct measurement of isotopic composition of interstellar noble gases probably can only be done with the foil collection technique. The *Genesis* mission of NASA, which currently is under construction, with launch foreseen for January 2001, uses this technique to collect solar wind. The *Genesis* spacecraft will be placed into orbit around L1†. Once in orbit, *Genesis* will unfold its wing-like arrays and begin collecting particles of the solar wind that will imbed themselves in specially designed high-purity wafers. After two years, the sample collectors will be re-stowed and returned to Earth. The main goal of the mission is to obtain precise measurements of solar isotopic abundances. *Genesis* will measure the isotopic composition of oxygen, nitrogen, and noble gases. These data will enable scientists to better understand the isotopic variations in meteorites, comets, lunar samples, and planetary atmospheres. Furthermore, it is planned to obtain greatly improved measurements of the elemental abundances in the solar wind.

The disadvantages of the foil collection technique are the limited spatial resolution (see discussion of the IGE/LDEF instrument) and the limited temporal resolution (on the order of one day). Furthermore, the fact that the instruments, or at least the foils, have to be brought back to Earth after exposure causes some complications for the mission. With the availability of space stations in Earth orbit the latter problem has almost been alleviated.

Just recently, foil collectors have been placed on the Mir space station. Two

†L1 is one of the five Euler-Lagrange points in the force field (gravitational and centrifugal forces) of the Sun and a planet (the Earth in this case) where the total force vanishes. Once a small object is placed there it will move in a circular orbit, always maintaining a fixed orientation to the two greater masses.

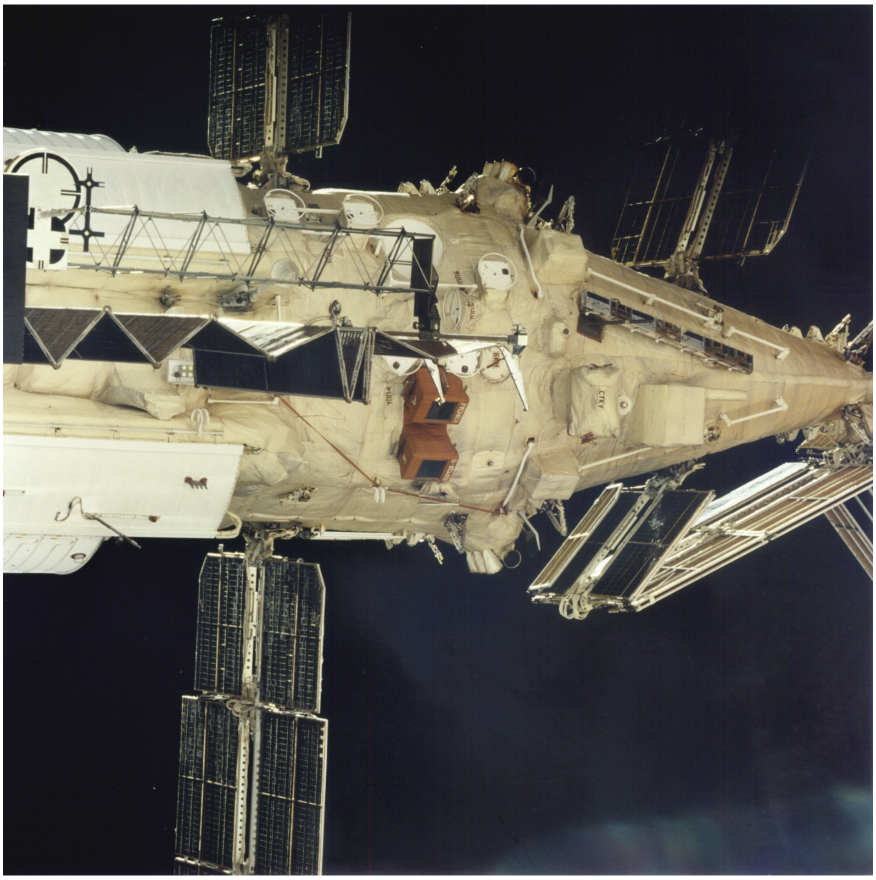

Fig. 7: Module Spektr of the Mir space station. The two foil collector units are covered by red Kapton thermal blankets (photo courtesy of NASA/Lyndon Johnson Space Center, STS071-701-059).

foil collector units are mounted on the outside of the Spektr module and remain there (see Fig. 7). The four collection foils (10 cm $\times$ 20 cm each) are mounted in cartridges loaded in the collector unit, which are exchanged by the Cosmonauts after exposure. These cartridges are brought back to Earth with the routine service flights. Several exposed foils have already been brought back to Earth and are currently under analysis (Bühler, 1999). There are plans to use the foil collection technique on Space Shuttle flights and also on the International Space Station to investigate the local interstellar gas.

4 Pinhole Cameras

Utilizing the pinhole camera concept, imaging is achieved by having incoming particles pass through a small aperture before impinging on an imaging detector located

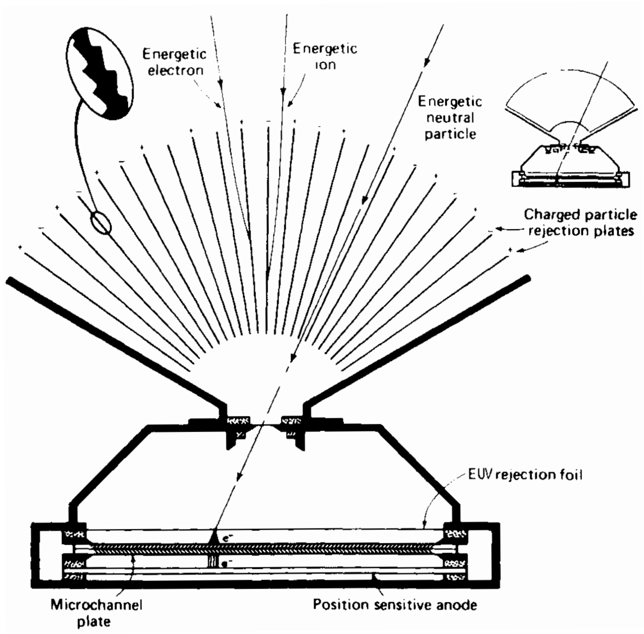

Fig. 8: Pinhole camera for ENAs (adapted from McEntire and Mitchell, 1989). An alternating potential on the charged particle deflection plates is applied to deflect energetic electrons and ions from reaching the detector. Plate surfaces are machined to inhibit forward scattering (detail upper left). A cut of the sensor in the other direction shows the shape of the rejection plates (detail upper right). An MCP detector with a position-sensitive anode is used to register the particles. An EUV blocking foil in front of the MCP detector attenuates the environmental EUV radiation to avoid saturation of the detector.

at a certain distance away from the pinhole. From the impact location on the detector in two dimensions the direction of the incoming particle can be calculated. By accumulation of registered ENAs for a certain time a two-dimensional image of the ENA flux is obtained directly without further processing.

A possible imaging instrument based on the pinhole camera concept is shown in Fig. 8. Neutral particles pass through the charged-particle deflection system and continue on to the pinhole. Voltages of alternating polarity are applied to the charged-particle deflection system to prevent electrons and ions from reaching the pinhole. Depending on the compromise between image resolution and the to-be-recorded signal intensity, the size of the pinhole may range from 1 mm^2 to 1 cm^2. After passing the pinhole, the neutral particles continue on a straight trajectory until they hit an EUV blocking foil. The impact of an ENA on the foil results in the release of secondary electrons on the backside of the foil, which then are registered on an imaging MCP detector. The EUV blocking is not necessary if a pixelized SSD is used (see below), since these detectors are not succeptible to photons in this energy range.

A variant of the pinhole camera is the slit imager, in which the pinhole is replaced by a slit. Thus, only one-dimensional images are recorded with the imaging axis perpendicular to the major axis of the slit. The imaging in the second dimension is then obtained by moving the slit over the object by the rotation of the spacecraft. The advantage of the slit imager over the pinhole camera is the substantially larger geometric factor. The PIPPI instrument of the ASPERA-C experiment on the Russian Mars-96 mission (Barabash et al., 1998) is such a slit imager with the slit wrapped around a circle of 360°. The PIPPI instrument has two channels: a PIPPI-MCP and a PIPPI-SSD channel for the energy ranges of 0.1–70 keV and 13–140 keV, respectively. With a spacecraft rotation perpendicular to the 360° viewing plane, full sky (4π sr) images are obtained.

Another variant of the pinhole camera is the coded aperture technique, where the single aperture is replaced by a two-dimensional array of apertures. Some of these apertures are open and some are closed. The exact pattern of this mask is given by a two-dimensional pseudo-random sequence (Gruntman, 1993a). Thus the object forms a multiplexed image on the imaging detector. The coded aperture technique has the advantage of a much larger aperture size and improved signal-to-noise ratio. However, this comes at the price of a more complicated instrument and an involved data deconvolution. A review of the coded aperture technique in the context of ENA imaging has been given recently by Gruntman (1993a). An instrument using a one-dimensional coded aperture has been proposed by Curtis and Hsieh (1989).

Since there is a direct optical path from the exterior through the pinhole to the detector, UV and EUV suppression are very important aspects of the instrument design. One measure for UV and EUV suppression is already indicated in the concept shown in Fig. 8, namely to have an EUV blocking foil in front of the imaging detector. This foil has to be thick enough to block the EUV photons efficiently but still be thin enough to allow the passage of ENAs without blurring the image. These conflicting demands result in blocking foils with only moderate photon suppression factors in the range of 10 to 10^3 depending on foil thickness (Hsieh et al., 1991). Moreover, the forward photoemission yield—that is photoelectrons released at the detector side of the EUV blocking foil—has to be considered, and is in the range of 10^{-2} to 10^{-5} also depending on foil thickness (Hsieh et al., 1980). The pinhole can be covered with an EUV blocking foil as well, but the image blurring due to particle scattering has to be considered. Thus, only for HENA instruments can the foil be thick enough to provide significant EUV suppression (see also Funsten et al., 1998). An alternative way to remove the photon flux from the ENA flux is to mount free-standing transmission gratings over the aperture; these suppress the UV photons without disturbing the incident neutral atom flux (Scime et al., 1994). A similar concept are the nuclear trac filters, which are thin films of 1–20 μm thickness with small channels with diameters varying from 4 nm to 10 μm (Gruntman, 1997).

So far, the pinhole camera does not provide any information on the mass or energy of the registered particles. Additional information is obtained by combining the pinhole imaging concept with a TOF measurement, or an energy measurement via a solid state detector, or even with both measurements (TOF-E sensors). These sensors will be discussed in detail below.

5 Imaging Detectors

ENA imaging depends in most cases on the detector's capability not only to register a particle but also to record its impact position on an extended detector surface. Basically, for particle detection two types of detectors are used nowadays: microchannel plate (MCP) detectors and solid state detectors (SSD).

5.1 Microchannel Plate Detectors

A MCP is a two-dimensional array of several million channels of 5–20 μm diameter (depending on model), which have a semiconducting surface coating inside the channel (e.g., Wiza, 1979; Fraser, 1989). Particles impinging on the channel wall create secondary electrons. These electrons are accelerated by an electric potential along the channel, which leads to charge multiplication. Typically, two MCPs are used in series to obtain amplifications on the order of 10^6. Since the detection principle of MCPs is based on the emission of secondary electrons upon particle impact, the detection efficiency exceeds the percent level only for particle energies above a few hundred eV (Brehm et al., 1995; Oberheide et al., 1997).

The electron cloud emitted by the MCP is collected on an anode, which for an imaging detector has to have a position-sensing capability. The common position-sensing systems rely on charge division on the geometrically extended anode. The different concepts are the resistive anode (Lampton and Carlson, 1979), the wedge-and-strip anode (Martin et al., 1981), and the crossed delay-line anode (Siegmund et al., 1994). Differences in these systems are the possible anode geometries, size of the anodes, read-out speed, and image resolution. For particle measurements the wedge-and-strip anode and lately the crossed delay-line anode are the most popular schemes. An alternative scheme is to divide the anode into many small pixels and to read out each of them individually. These imaging detectors use a single, curved MCP for the charge amplification and are known as the multi-anode microchannel array (MAMA) detectors (Timothy et al., 1981).

Microsphere plates (MSP) are sintered disks of glass beads (Tremsin et al., 1996). The principle of MSPs is similar to MCPs, however the electron amplification is along the openings left between the beads of the plate. Either two MSPs are used in series or one thick MSP is used. Modal gains in the range of 10^7 to 10^8 are achieved. MSPs are mechanically more robust than MCPs and can also easily be machined to special shapes. Currently, MSPs are being investigated by several groups for possible use in space instrumentation.

Channel Electron Multipliers (CEM) are the predecessors of MCPs. A conventional CEM consists of a semiconductive glass channel having an inner diameter of a few millimeters and a length-to-diameter ratio of 50:1 or greater (Burrows et al., 1967). Modal gains are in the range of 10^6 to 10^8. CEMs have been used widely in space instrumentation since the early 60's because of their simple implementation and high reliability. Since CEMs have no imaging capability they can only be used for telescopes, which limits their application in this field.

5.2 Solid State Detectors

An energetic particle penetrates a SSD and loses most of its energy in Coloumb collisions with free and bound electrons (Bertollini and Coche, 1968; Knoll, 1989). The deposited energy results in the creation of electron-hole pairs. In silicon it takes 3.62 eV to create such an electron-hole pair at room temperature. By applying an electric field across the SSD detector, the created charge carriers drift to contacts of opposite polarity. By measuring the total collected charge collected on one contact one can determine the energy deposited by the particle. Solid state detectors are available since 1960. First the Silicon Surface Barrier (SSB) detectors and Diffused Junction (DJ) detectors became available. Since 1980, Passivated Implanted Planar Silicon (PIPS) detectors are available, which have several advantages over comparable SSB and DJ detectors. The biggest advantange of PIPS detectors is the reduced dead-layer (window) thickness. PIPS detectors typically have a window thickness of $<$ 500 Å, SSB detectors with an Au window have a window thickness of $\approx$ 800 Å, and SSB detectors with an Al window have a window thickness of $>$ 2000 Å (all thicknesses are equivalent to Si). Also, the leakage current of PIPS detectors is typically 1/10 to 1/100 of that of SSB and DJ detectors. Both features result in lower achievable detection thresholds. Best results at room temperature for X-rays are a threshold at 1.0 keV and an energy resolution of 1.5 keV. For particles the lowest possible threshold is currently around 10 keV.

Cooling of SSDs to temperatures of –50° C will further reduce leakage current and the electronic noise, and hence improve energy resolution. The energy threshold will also be improved (or reduced). A lower limit of the threshold, however, is given by the window thickness and hence depends on the particles to be measured.

To obtain an image with a SSD one divides the active area of the detector in many discrete pixels, which are read out individually. Typically, a pixel size of $> 1 \times 1$ mm^2 can be achieved with gaps between the pixels of about 0.1 mm. Solid state detectors with discrete pixels are called pixelated SSDs (PSSD). Such detectors have been used in the IMS-HI instrument on the CRRES spacecraft (Voss et al., 1993) and in the CELIAS instrument on the SOHO spacecraft (Hovestadt et al., 1995). For ENA imaging, SSDs have the big advantage that they are immune to UV and EUV radiation, since the photon threshold is at 1.0 keV. Furthermore, the energy of the detected particle is measured. However, SSDs are slow and cannot be used directly for time-of-flight systems.

6 The Ulysses GAS Instrument

The aim of the Ulysses GAS instrument is to directly measure *in situ* the kinetic parameters of the flow of interstellar gas. Although the flux of neutral interstellar atoms near the Earth's orbit is $> 10^4$/(cm^2 s) under favorable observation conditions, it is difficult to detect these neutral particles. Usually, neutral particles to be measured are ionized first, and then their energy and direction are determined by common energy-per-charge or mass-per-charge analysis. However, at the high velocities of these atoms with respect to the spacecraft (some 10 km/s), the ionization

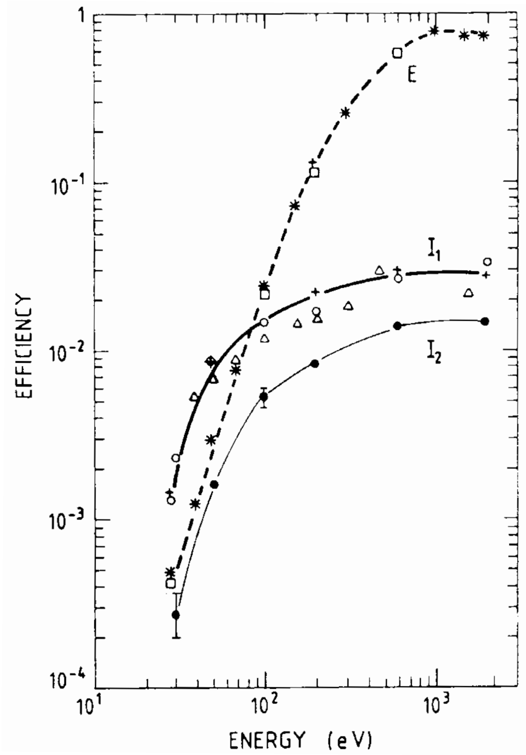

Fig. 9: Efficiencies for the production of secondary electrons (E) and secondary ions (I_1) as a function of energy of impacting helium atoms, measured several times after the deposition of a LiF layer (2 hours to 6 days). Curve (I_2), measured after the LiF layer had been exposed to air for about a month, shows that in the "worst" case of contamination the efficiency degrades only by a factor of two (from Witte et al., 1992).

probability for an electron-impact ionization source is only on the order of 10^{-5} to 10^{-6}. Therefore, one has to use a different technique for particle detection. In the Ulysses GAS instrument the emission of secondary particles from a conversion plate by the impinging interstellar atoms is used. This instrument has been described in detail by Witte et al. (1992).

The impact of energetic particles on a solid surface causes the emission of electrons (secondary electrons) and the emission of atoms and ions from the solid surface (sputtering). Both secondary electron and secondary ion emission are suitable detection mechanisms. The problem with secondary electron emission is that photoelectrons can seriously disturb the measurement. Secondary ion emission usually has the disadvantage of a rather small yield. It was found that lithium fluoride (LiF) has a low photoelectron yield since its bandgap is 14.2 eV; thus it is transparent even to H Lyman α radiation. Moreover, since LiF is an ionic crystal, the ion yield (especially of Li^+) is reasonably high. The efficiencies for the production of secondary electrons and secondary ions are shown in Fig. 9 for helium atoms.

Both processes are strongly energy dependent. At energies around 80 eV both efficiencies are about 10^{-2}; toward lower energies the efficiencies fall off rapidly. Therefore, an instrument based on the LiF conversion technology is only useful for neutral helium detection if the particle energy is above $\approx$ 30 eV, corresponding to an impact velocity of $\approx$ 27 km/s for He. This means the trajectory of the

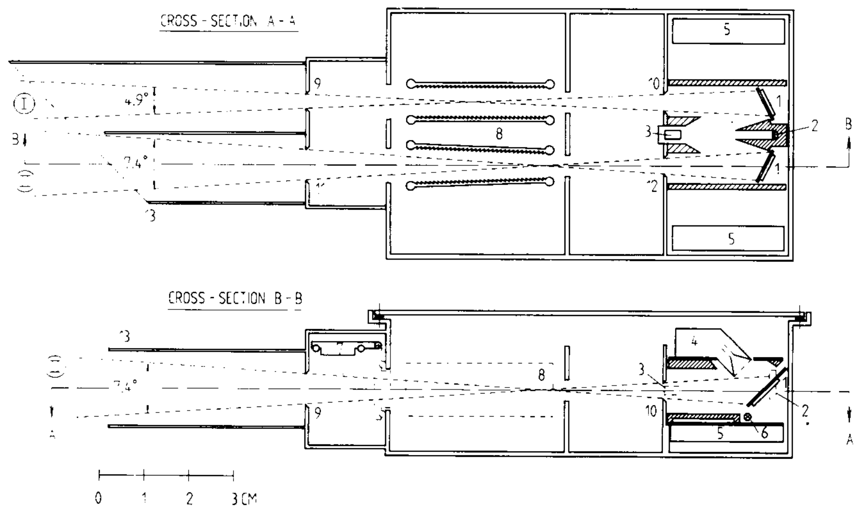

Fig. 10: Cross-sections of the sensor head of the Ulysses GAS instrument. 1) conversion plate with heater, evaporated with lithiumflouride (LiF), 2) quartz crystal for monitoring the LiF evaporation process, 3) furnace with LiF supply, 4) channel electron multiplier (CEM), 5) CEM-amplifier and electronics, 6) tungsten filaments to stimulate the CEMs, 7) vacuum-tight cover in closed (dashed lines) and open position, 9 & 10) circular apertures defining the field-of-view of channel I, 11 & 12) circular apertures defining the field-of-view of channel II, 13) light baffle (from Witte et al., 1992).

spacecraft needs to be such that, at least for a certain time during the mission, the relative velocity of the spacecraft with respect to the interstellar gas clearly exceeds the 27 km/s needed to be able to make useful measurements. Hydrogen, the most abundant element in the interstellar gas, has a significantly lower secondary ion yield than helium due to its lower mass. Moreover, because of the rapid fall-off of the efficiencies with energy, which for all elements is similar to helium, the secondary yields are very low and this detector is essentially blind for hydrogen of the interstellar gas. Heavier atoms are detected efficiently, but their abundances in the interstellar gas are very small (see Chapter 2.2.2). Thus most of the signal detected by the Ulysses GAS instrument is due to neutral interstellar helium.

A schematic representation of the Ulysses GAS instrument is given in Fig. 10. The instrument consists of two nearly identical detector channels, housed in a vacuum-tight box. The field-of-views are limited by two circular apertures in each channel. The full opening angle is 4.9° in channel I and 7.4° in channel II. The outer apertures are protected by a simple asymmetric baffle system against direct sunlight. Incoming particles first pass electrostatic deflection systems, which serve as filters against charged particles up to energies per charge of ≈ 80 kV in channel I and ≈ 50 kV in channel II. The neutral particles continue to impact on the conversion plates, which measure about 8 mm $\times$ 10 mm and are inclined by 45° to the optical axis toward the channel electron multipliers (CEM) and by 28° toward the furnace. By heating the furnace mounted in the middle between the two channels, high-purity LiF is evaporated and new layers are deposited simultaneously on both

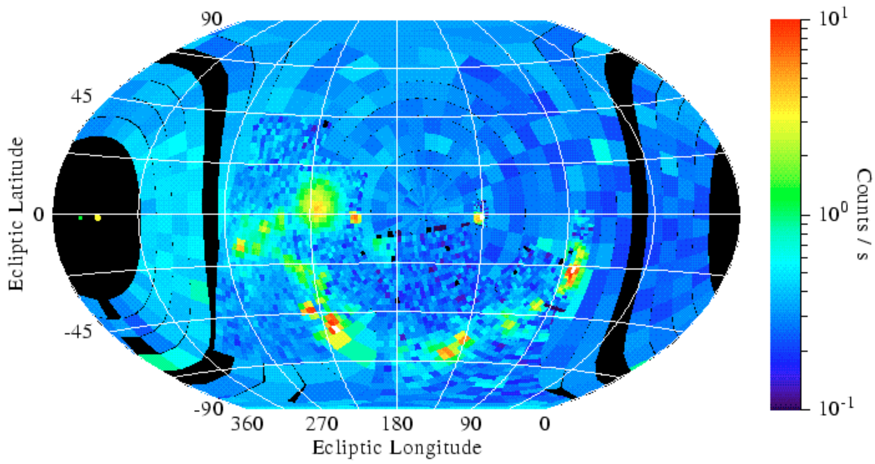

Fig. 11: A composed picture of the heliosphere as seen by the Ulysses GAS instrument in January 1992 inbound to Jupiter. The flow of interstellar neutral helium appears as the blurred spot at longitude $\lambda \approx 225°$ and latitude $\beta \approx 5°$. The neutral particle emission from Jupiter can be seen at $\lambda \approx 135°$ and $\beta \approx -1°$. A chain of UV-emitting stars along the galactic plane can be seen in the southern hemisphere. The positions of the Sun (large dot), and the Earth (small dot) are indicated in the blank area on the left side (from Witte et al., 1993).

conversion plates. A small quartz crystal monitor checks the thickness of the applied layers. Secondary charged particles released from the conversion plate upon impact of an incoming particle are accelerated to the CEMs and counted by conventional electronic means. Depending on the polarity of the accelerating potential, either secondary electrons or secondary ions are registered.

In principle, the Ulysses GAS instrument acts like a pinhole camera. However, the instrument does not have an imaging detector, thus it has to be scanned over the whole sky in two dimensions to obtain pictures of neutral helium flux. The whole celestial sphere can be scanned by using the spacecraft rotation and an instrument-provided mechanical stepping platform to point the sensor's optical axis to different cone angles. Angular resolutions (pixel size) between $0.7° \times 1°$ and $11° \times 8°$ can be selected. Figure 11 shows a scan over the whole celestial sphere with varying angular resolution. Several different objects are observed: the neutral particles from the interstellar helium flow, and also those from Jupiter; the UV radiation from stars; and the resonantly scattered sunlight from the neutral particle component in the heliosphere, which is the slightly varying background (see Chapter 2.3.3). These data were taken in January 1992 when Ulysses was approaching Jupiter (Witte et al., 1993).

The advantages of the Ulysses GAS instrument are the rather simple design and the simple operation in space. Also, the detection efficiency for energetic helium atoms in the energy range of the interstellar gas is high, and there is probably no other technique with a comparable detection efficiency for helium. The disadvantage of the Ulysses GAS instrument is that no mass and energy analysis is possible. If the composition of analyzed ENAs and the energy range do not fit so favorably with the characteristics of this instrument, the extraction of meaningful data will be difficult, perhaps even impossible. So far the Ulysses GAS instrument is the only instrument of this kind realized for a space research application. However, for future missions to investigate the interstellar gas it is very likely that an instrument of the Ulysses GAS type will be part of the scientific instrument complement for the measurement of the inflowing interstellar helium atoms. One can imagine that the experimental technique will be extended to be a full pinhole camera with a position-sensitive detector. This would alleviate the need for a scan platform and for a spinning spacecraft.

7 TOF Instruments

For the identification of energetic particles, time-of-flight (TOF) spectrometers are almost always used today. The advantages of TOF spectrometers are manyfold. One outstanding advantage is the high sensitivity, since TOF spectrometers are non-scanning instruments recording particles of all masses and energies at the same time (unlike, e.g., quadrupole and sector magnet instruments). TOF instruments are simple to design and to build, and easy to operate. TOF instruments can be built very small and light-weight. Furthermore, the coincidence measurement inherent to the TOF measurement principle provides good background suppression.

TOF instruments designed to detect and image ENA fluxes share many characteristics with TOF instruments designed for energetic charged particle detection in space. However, since ENAs are not deflected by electric or magnetic fields, ENA imagers all rely upon straight path optical techniques and detectors sensitive to fast particles. In addition, the generally low flux of ENAs requires instruments with large geometric factors and large detectors. Furthermore, particular attention has to be paid to the rejection of charged particles and the UV suppression.

7.1 Principle of TOF Spectrometers

In TOF instruments, an incoming particle is identified by having it pass through a thin start-foil (typically of 100 Å thickness) to produce a start signal and then by measuring the elapsed time until the particle hits a stop detector at a given distance. For the start and stop signals the secondary electrons released upon passage of the particle through the start-foil and upon impact on the stop detector are used. This type of spectrometer, also called a linear TOF mass spectrometer because particles move along a straight path between the start and the stop plane, was first proposed for measurements in space by Gloeckler and Hsieh (1979), and has successfully been employed since then in many instruments on space missions.

Most of the time carbon foils (basically graphite foils) with thicknesses ranging from 50 Å to 500 Å are used for the start foil. In certain situations composite foils adapted to meet particular requirements are used (Hsieh et al., 1991; Mitchell et al., 1993; Hovestadt et al., 1995). Recently, diamond-like carbon (DLC) has been investigated as a material for the start-foil (Ivkova et al., 1995). DLC foils have the advantage of about 100 times the tensile strength of carbon foils, and also have a

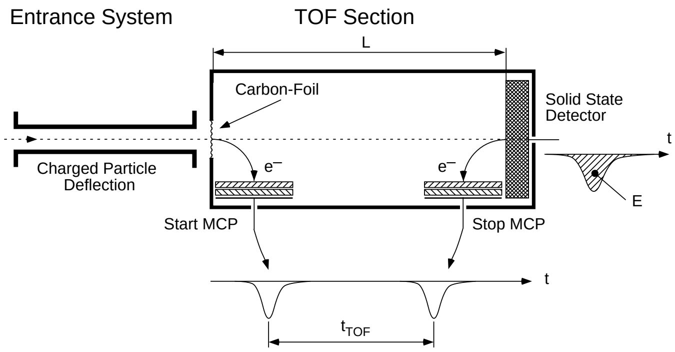

Fig. 12: Schematic view of a carbon-foil time-of-flight mass spetrometer.

higher secondary electron yield.

The principal components of a TOF spectrometer are the start-foil (carbon foil), a field-free drift path for the particles, secondary electron extraction optics, and two MCP detectors (start and stop detector). The full instrument consists of a TOF section and a collimating system, shown schematically in Fig. 12. TOF spectrometers can be built very easily to be pinhole cameras, with the pinhole being covered by the start-foil.

The time-of-flight measurement gives the velocity of the particle. Such a TOF measurement is a coincidence measurement since one needs a start and a stop signal for a successful identification of a particle. By setting a window of allowed time-of-flights one can discriminate against particles being too fast (too energetic) or too light (e.g., electrons). Such a coincidence measurement also discriminates well against background induced by photons, since these mostly generate a start pulse (sometimes a stop pulse) but never a start and a stop pulse. However, one has to make sure that the background induced by the photon flux does not saturate the electronics and does not degrade the start detector due to a high flux. High fluxes of background radiation can cause accidental coincidences—that is, a particle (photon) creates a start pulse and another particle generates a stop pulse. This will look to the electronics like a valid TOF measurement and will be recorded as such.

If a solid state detector (SSD) is used as stop detector, the energy of the particle is also measured. This measurement is called a triple-coincidence, since it needs three measurements for the successful identification of a particle. The suppression of any background sources is even better than for the coincidence measurement. These sensors are called TOF-E sensors since they combine a velocity measurement and an energy measurement. From the measurement of the time-of-flight, T_{TOF}, and the measurement of the particle energy with the SSD, E_{SSD}, we get the mass, m, of the particle as

$$m = 2E_{SSD} \left(\frac{T_{TOF}}{L_{TOF}} \right)^2 \tag{4}$$

for a TOF sensor with a length of the field-free path of L_{TOF}. Depending on the desired energy range and mass resolution needed, the length of the field-free path is a few cm to about 20 cm. The mass resolution of a time-of-flight mass spectrometer is derived from eq. 4 by

$$\frac{\Delta m}{m} = \frac{\Delta E_{SSD}}{E_{SSD}} + 2\frac{\Delta T}{T_{TOF}} \tag{5}$$

For a passivated implanted planar silicon used in the CTOF sensor of the CELIAS instrument the energy resolution was found to be (Oetliker, 1993)

$$\frac{\Delta E_{SSD}}{E_{SSD}} = 875 \left(\frac{E_{SSD}}{m}\right)^{-0.92} \tag{6}$$

where E_{SSD} is the incident energy of the particle in [eV] and m the mass of the particle in [amu]. The time resolution of a carbon foil TOF spectrometer is given as the sum of several factors that limit the accuracy of the time measurement

$$\left(\frac{\Delta T}{T_{TOF}}\right)^2 = \left(\frac{\Delta T_e}{T_{TOF}}\right)^2 + \left(\frac{1}{2}\frac{\Delta E_{foil}}{E^*}\right)^2 + \left(\frac{\Delta L_{foil}}{L_{TOF}}\right)^2 + \left(\frac{\Delta L_{FOV}}{L_{TOF}}\right)^2 \tag{7}$$

where T is the total flight time of a particle on the field-free path of length L_{TOF}. E^* is the kinetic energy of the particle after passing the carbon foil, which is less than the energy before the foil because the particle suffered a loss of its kinetic energy due to interaction of the particle with the solid (see Betz and Wien, 1994, and references therein). The energy measured by the SSD is E^* minus an energy defect arising from the dead-layer of these detectors. ΔT_e is the resolution of the time measuring system, ΔE_{foil} is the energy straggling in the carbon foil, ΔL_{foil} is the variability of the flight path resulting from angular scattering in the carbon foil, and ΔL_{FOV} is the variability of the flight path due to the range of angles allowed by field-of-view defined by the entrace collimator. The contribution from the time measurement uncertainty is simply

$$\frac{\Delta T_e}{T_{TOF}} = \frac{\Delta T_e}{L}\sqrt{\frac{2E^*}{m}} \tag{8}$$

Particles passing the carbon foil not only suffer energy loss, but also energy scattering, which limits the resolution of a TOF sensor. For carbon, the energy scattering can be estimated as (Echenique et al., 1986; Beiersdorfer et al., 1987)

$$\frac{\Delta E_{foil}}{E} \approx 3.6\sqrt{s\frac{m}{E}} \tag{9}$$

where E is the incident energy of the particle in [eV], m is the mass of the particle in [amu], and s is the thickness of the foil in [μg/cm^2]. Typically, these carbon foils have a thickness between 1.0 μg/cm^2 and 5.0 μg/cm^2 (corresponding to about 50 Å to 250 Å). The contribution due to angular scattering in the carbon foil is given by

$$\frac{\Delta L_{foil}}{L_{TOF}} = \left(\frac{1}{\cos\psi_{1/2}} - 1\right) \tag{10}$$

with

$$\psi_{1/2} = 12.0 \cdot 10^3 \left(Z_1^{3/4} \frac{s}{E} \right) \tag{11}$$

with $\psi_{1/2}$ being the half-width of the distribution of scattering angles in [°] (Bernstein et al., 1970; Högberg et al., 1970). Z_1 is the atomic number of the projectile and s is again the thickness of the carbon foil in [μg/cm^2]. Since the angular scattering increases for lower energies, this sets a limit to the useful energy range of a TOF sensor with a start-foil (carbon foil). Also, if the TOF sensor is part of an imaging instrument, the image resolution will severely degrade at energies below 1 keV/nuc. Furthermore, the energy loss also increases with the scattering angle (Beauchemin and Drouin, 1975), which causes the TOF peaks in the spectrum to be wider on the side of higher time-of-flights.

Figure 13 shows the calculated time resolution for hydrogen atoms for a typical TOF sensor as a function of the energy-per-nucleon. At low energies the time resolution is dominated by the energy straggling in the carbon foil, and at the lowest energies the angular straggling further reduces the time resolution. At higher energies the time resolution is limited by the resolution of the time measurement system. At intermediate energies there is a minimum of $\Delta T/T$ that means there is a maximum in mass resolution of $m/\Delta m \approx 15$ in this example, which is a little bit higher than can be realized in actual instruments. For heavier atoms the time resolution looks similar to the hydrogen case when plotted against energy-per-nucleon, but the maximum mass resolution is somewhat higher (because of eq. 9). If higher mass resolution is desired (e.g., for isotope analysis), an isochronous TOF mass spectrometer instead of the linear TOF instrument has to be used (Gubler et al., 1995; Wurz et al., 1998). However, a design which combines ENA detection and isochronous TOF mass spectrometers has not been done until now, but will be necessary for the investigation of isotopic compositions.

Figure 14 shows solar energetic particle data from a coronal mass ejection (Bamert, 1999) recorded with a TOF-E instrument to illustrate the performance that can be obtained with such an instrument. Data were recorded with the STOF and HSTOF sensors of the SOHO/CELIAS instrument (Hovestadt et al., 1995). The instrument clearly separates the major species down to energies of ≈ 30 keV. The lower limit of the energy range is given by the energy threshold of the SSD and the electronic noise. Therefore, TOF-E instruments are all in the HENA energy range. On the high energy side, the energy range is limited by the smallest time that the time-measuring electronics can measure reliably. Typically this limit is at an energy of a few MeV, which is also the high-energy limit imposed by the charged particle deflection systems (see Chapter 2.3.1). Although it is not a dedicated ENA instrument, energetic hydrogen atoms of heliospheric origin in the energy range from 55 keV to 80 keV could be detected with the HSTOF sensor of the SOHO/CELIAS instrument (Hilchenbach et al., 1998).

If one omits the SSD detector for the energy measurement one can extend the energy range of a TOF instrument to lower energies, covering the MENA range. The next item, which limits the energy range at the low energy side, is the carbon foil. The TOF measurement relies on the secondary electron yield γ and on the transmis-

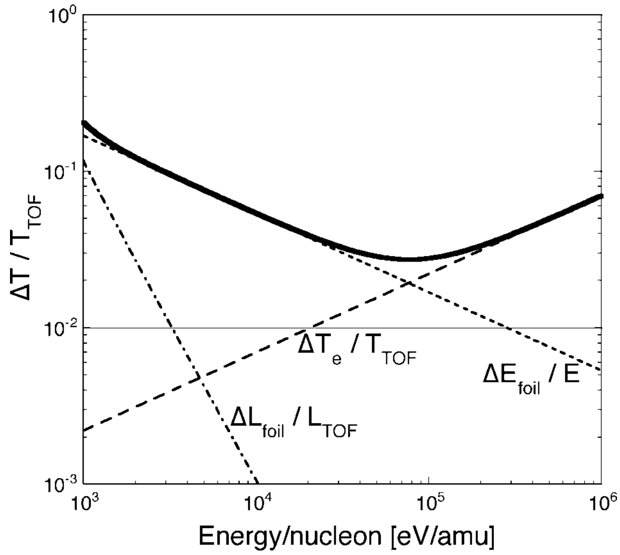

Fig. 13: Time resolution (bold line) for a linear TOF spectrometer as obtained from eq. 7 for hydrogen. The parameters are s = 2.2 μg/cm^2, ΔT_e = 0.5$\cdot$10^{-9} s, and L_{TOF} = 10 cm. The three contributions arising from the resolution of the time measurement, from the energy scattering in the carbon foil, and from the angular scattering in the carbon foil are indicated; a contribution by the field-of-view is not considered.

sion of the particle through the carbon foil, which are shown in Fig. 15 for oxygen (Wurz, 1999). Note that the secondary electron yield on the exit side of the carbon foil is shown (also called forward emission), since in most TOF instruments these electrons are used for triggering the TOF measurement (see Fig. 12). Assuming a Poisson distribution, the start efficiency is calculated from the secondary electron yield by

$$\epsilon_{start} = 1 - e^{-\mu_{MCP} \cdot \gamma} \tag{12}$$

for a typical detection efficiency of μ_{MCP} = 0.6 for a MCP detector. Particles need a certain amount of energy to pass through a carbon foil of a finite thickness, which results in a threshold-like behavior for the secondary electron yield and for the carbon foil transmission. This threshold is located around 300 eV/nuc, which varies with element and foil thickness. Moreover, one has to consider the angular scatter in the carbon foil, which will result in a considerable loss in particle flux to the detector, since particles are scattered too much at low energies according to eq. 11. Also, the imaging capabilities will be severely degraded at energies close to the threshold. This means that the effective energy range of such instruments starts around 1 keV/nuc. One can try to push this limit to lower energies by using “ultra-thin” carbon foils with thicknesses of 0.5 – 1 μg/cm^2, but the reliability of these foils in a space-flight situation is very questionable.

Since we gave up the energy measurement we have to find some other way to infer the mass of the recorded particle. Since the secondary electron yield is a function of

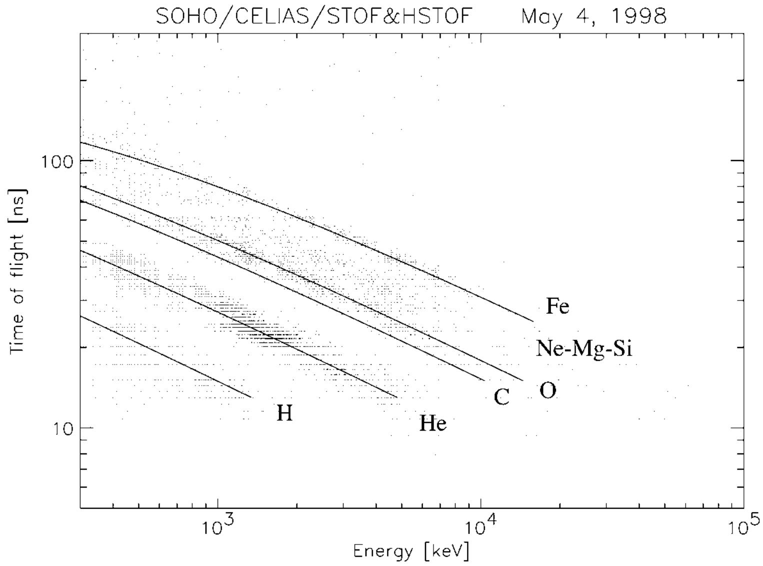

Fig. 14: Time-of-flight versus energy matrix of ions associated with the coronal mass ejection of May 4, 1998, recorded with the SOHO/CELIAS instrument (from Bamert, 1999). Tracks of protons, helium, carbon, oxygen, the neon-magnesium-silicon group, and iron can be seen. The TOF-E technique clearly separates the major species down to energies of $\approx$ 30 keV. The solid lines give the nominal position of a measurement in the time-of-flight versus energy matrix.

mass, at the same velocity, pulse height analysis of the secondary electron yield will allow us to infer the mass of the registered particle. Figure 16 shows the secondary electron yield of carbon upon particle impact for several elements. The pulse height analysis will allow the distinction between the two major plasma constituents H and O, but minor species will not be resolved easily. Thus, the technique provides only a limited “mass resolution”, but for many applications dedicated to atmospheric or magnetospheric research this resolution is sufficient.

7.2 The HENA/IMAGE Instrument

As an example of an actual instrument, we want to briefly discuss the HENA instrument of the IMAGE mission, since it has all the components we discussed above and it is probably the most advanced instrument of its kind (Mitchell et al., 2000). For a review of current and past HENA instrumentation see McEntire and Mitchell (1989) and the general review by Gruntman (1997).

The HENA instrument is a further development of the INCA instrument on the *Cassini* mission (Mitchell et al., 1993). The HENA sensor consists of alternately charged deflection plates mounted in a fan configuration in front of the entrance slit, three MCP detectors, two pixelated SSDs, two carbon-silicon-polyimide foils (one at the entrance slit and the other placed just in front of the back MCP) and a series of wires and electrodes to steer secondary electrons released from the foils (or the

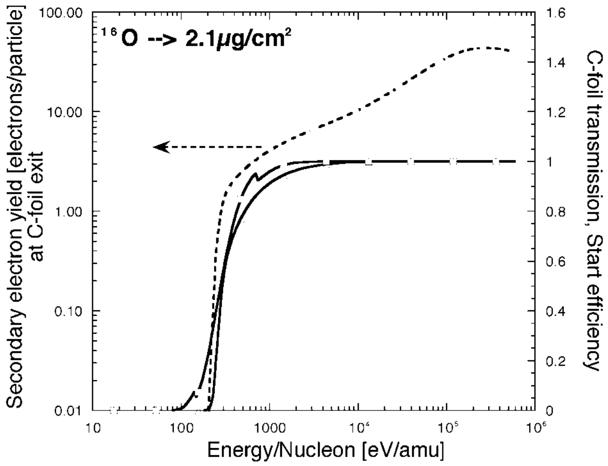

Fig. 15: Calculated yield of secondary electrons emitted on the exit side of the carbon foil upon passage of an ^{16}O atom through a carbon foil of 2.1μg/cm^2 thickness (dashed line, left y-axis). The detection efficiency for a typical MCP start detector (open squares, right y-axis) and the transmission through the carbon foil (open triangles, right y-axis) are given (from Wurz, 1999).

SSDs) to the start and stop MCPs. Power for the MCPs and deflection plates and for secondary electron steering is provided by high-voltage power supplies that reside with the sensor. Figure 17 shows a schematic drawing of the HENA instrument.

When an incoming ENA passes through the start foil, it produces secondary electrons, which are accelerated and steered to the 1-D imaging start MCP. This MCP provides a start signal for the TOF analysis and registers the position at which the ENA penetrated the entrance slit. The ENA then continues through the sensor to the backplane and strikes either the stop foil in front of the 2-D imaging stop MCP or the SSD. In the first case, secondary electrons ejected from the stop foil trigger a stop pulse in the 2-D imaging MCP, which also registers the position of the incident ENA. If the ENA strikes the one of the SSDs instead, the released secondary electrons are steered to the coincidence MCP, which provides the TOF stop signal. The position of impact is registered by the SSD.

The start and stop pulses give the ENA's time of flight, while the position measurements reveal its trajectory and thus its path length within the sensor. With these two pieces of information, time of flight and path length, HENA can calculate the ENA's velocity. The energy of the incident ENAs is measured with the SSD. From the velocity and the energy measurements the mass of the registered particle is calculated using eq. 4. Calculating mass from the velocity and the SSD energy measurement is the primary technique used by HENA to determine composition of the ENAs. A second technique uses the pulse height of the MCP signal to distinguish between O and H, the two most common neutral atoms expected in the magnetosphere.

8 Instruments Using Surface Effects

To make ENA measurements in the LENA energy range—that is, in the energy range between 10 eV and 1 keV—one needs detection techniques different from the ones discussed above. Since particles of such low energy cannot pass through even

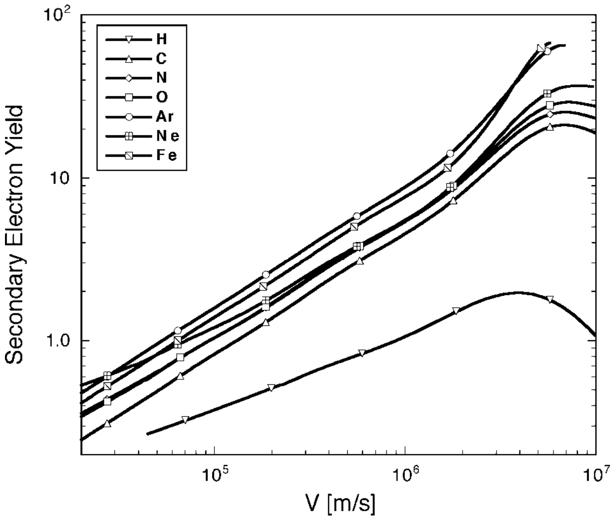

Fig. 16: Calculated yield of secondary electrons emitted upon particle impact on a carbon foil versus the particle velocity for several elements (from Wurz, 1999).

the thinnest foils anymore, one uses the interaction of a particle with a suitable surface upon scattering to initiate detection. Using the particle interaction with surfaces for ENA detection was first proposed by Herrero and Smith (1992). Currently, two methods are pursued for particle detection based on surface scattering: secondary electron emission and surface ionization. The former method is currently being developed for the ASPERA-3 instrument on the Mars Express mission; the latter method is applied in the LENA instrument on the IMAGE mission. Both methods and the respective instruments are discussed in some detail below.

In order not to absorb the particles in the surface, and also to achieve specular reflection of the scattered particles, a shallow angle of incidence with respect to the surface has to be chosen. Nevertheless, particles scattered from surfaces also experience angular and energy scatter, similar to the angle and energy scatter particles suffer when passing through thin foils. Particles also suffer energy loss upon reflection from the surface. Although the scatter is less than for carbon foils at the same energy, it is still considerable and has to be taken into account in the instrument design. Since the scattered particle probes the surface on atomic length scales, the surface has to be smooth on these length scales, otherwise the angular and energy scatter will be substantial. This means that the surface has to be polished as well as can be done; an optical mirror finish is not enough. The angular scatter is shown in Fig. 18 for a highly polished tungsten single crystal of orientation (110) for an angle of incidence of 82°. This surface had been polished to a smoothness of < 30 nm$_{rms}$ and probably represents the best that can be achieved today. In an actual instrument, the angle of incidence would be steeper, and the scatter grows non-linearly with increasing angle to the surface (Schletti, 1996). Also, the fraction of particles scattered around the specular direction is considerably less than 100%. For the surface used for the measurement in Fig. 18 it amounts to about 30%, which is again on the high side compared to other highly polished surfaces from different elements (Jans, 1999).

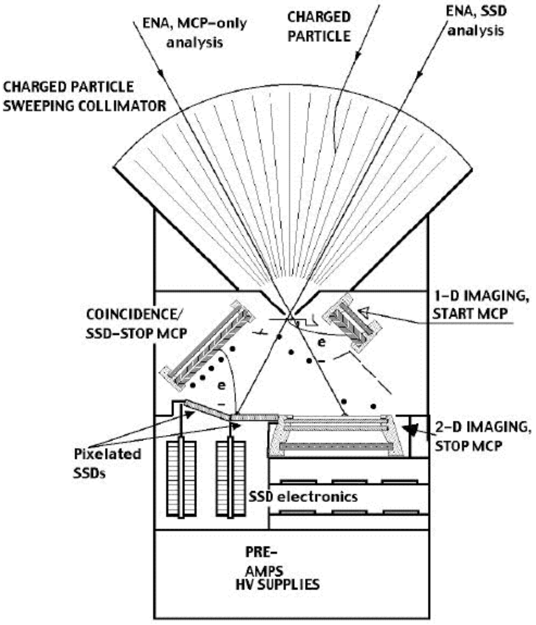

Fig. 17: Schematic drawing of the HENA instrument on the IMAGE mission (from Mitchell et al., 2000). Electrically-biased and serrated collimator plates provide the electric field to sweep charged particles out of the entrance slit. ENAs penetrating the start foil produce secondary electrons which trigger the 1-D imaging start MCP. The ENAs continue to travel to either the SSD or the back foil with the 2-D imaging MCP directly behing it. Secondary electrons released either at the SSD or the back foil are steered to the coincidence/SSD-stop MCP. The dots indicate the locations of the wires for steering the secondary electrons to the respective MCPs. The spacecraft spin vector is perpendicular to the plane of the figure.

8.1 Detection Based Upon Secondary Electron Emission

This detection method uses the emission of secondary electrons upon the scattering of a particle from a suitable surface. The release electron serves as the start event for a TOF measurement, similar to the way the carbon foil is used in the TOF instruments discussed above. The time-of-flight gives the particle's velocity. The mass of the registered particle will be inferred from pulse-height analysis of the start and the stop secondary electron yield (see Fig. 16). The "mass resolution" of the sensor will make it possible to distinguish between the two major constituents of the plasma H and O, but minor species will not be resolved easily. The energy dependence of the secondary electron yield limits this technique at low particle energies to about 100 eV. Note that grazing incidence on the start surface results in higher secondary electron emission than at normal incidence (Hasselkamp, 1991).

The Neutral Particle Detector (NPD) sensor of the ASPERA-3 instrument on ESA's Mars Express mission is such an instrument (Lundin et al., 1998). The NPD sensor consists of two identical units, each of which is a 1-D pinhole camera with a 90° field-of-view, and a combined field-of-view of 180°. Figure 19 provides a three-dimensional schematic view of the two NPD units along with an ENA trajectory. In each unit the charged particles—electrons and ions—are removed by an electrostatic deflection system which consists of two 90° sectors separated by a 4.5 mm gap. The deflection system is also equipped with broom magnets to remove electrons (not shown in Fig. 19). During normal operations a voltage of 8 kV will be applied to the plates of the sectors, and the resulting electric field strength sweeps away all charged particles with energies up to 70 keV (see discussion in Chapter

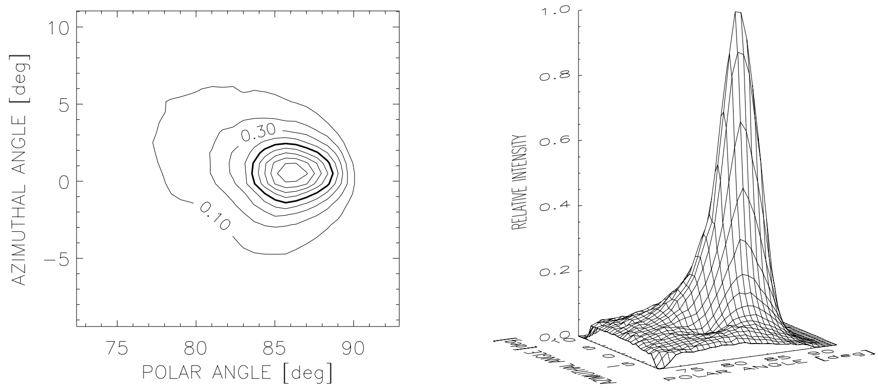

Fig. 18: Angular scattering of oxygen ions from a single crystal tungsten surface of orientation (110) at an angle of incidence of 82° (measured from the surface normal).

2.3.1). The collimator also collimates the incoming neutral beam in elevation angle. A collimated ENA beam emerges from the pinhole (4.5×4.5 mm^2), hits a start surface under grazing angle of incidence and causes the emission of secondary electrons. By a system of electrically biased grids, these electrons are collected and transported to the start MCPs on either side of the start surface. The neutral particles are reflected from the start surface nearly specularly and continue their trajectory to hit a stop surface. Secondary electrons emitted upon impact are accelerated onto a stop detector, which also registers the impact location in one dimension, and therefore the azimuth information of the incoming ENA. The stop surface is specially coated to provide high secondary electron yield and low UV photoelectron yield. This is accomplished by using a coating of a high bandgap material (e.g., magnesium oxide). The UV suppression in the NPD sensor is facilitated by the start surface and moreso by the stop surface. The stop surface can be mechanically rough, with a corrugation of the same characteristic length as the wavelength of the UV photons. This will minimize the number of specularly reflected photons and enhance the total photon suppression. Also, the coincidence measurement of start and stop helps to reduce the background.

The advantages of this technique are a simple, light-weight, and small design and easy operation in space. The NPD sensor of the ASPERA-3 instrument on the Mars Express mission will only weigh about 2 kg, which is fairly low for an imaging mass spectrometer. The ability to distinguish between H and O atoms is anticipated. The image resolution will be best in the direction scanned by the rotation of the spacecraft, since it is geometrically defined by the field-of-view of the entrance collimator. In the other direction where the sensor detemines the arrival direction of the particles the image resolution will be limited by the angular scattering on the start surface (see Fig. 18).

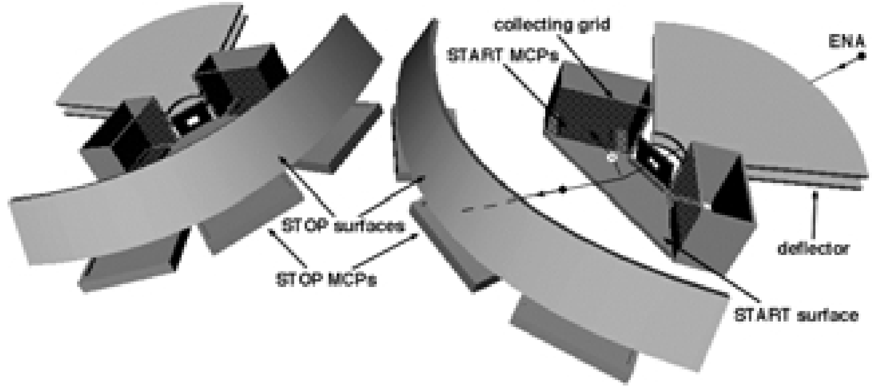

Fig. 19: Three-dimensional view of the principal components of the NPD sensor of the ASPERA-3 instrument on ESA's Mars Express mission (from Lundin et al., 1998).

8.2 Detection Based Upon Surface Ionization

Direct detection of neutral atoms with energies below a few hundred eV is not feasible. Secondary electron emission, on which most of the particle detectors rely, gives useful electron yields only at particle energies in excess of a few hundred eV. SSD detectors have even a much higher energy threshold for particle detection. Therefore, conversion of the atoms into charged particles is necessary. Once ionized, these particles can be subjected to the common energy-per-charge and energy-per-mass analysis, and accelerated toward a particle detector.

One way of achieving conversion is to strip off an electron from the neutral atom in a gas cell. Because the stripping efficiencies drop considerably below 200 eV (Fleischmann and Young, 1969), this technique is not feasible for the indicated energy range. The only method known so far to obtain reasonable conversion yields is surface ionization, where neutral atoms are converted to negative ions upon reflection from a suitable surface. Of course, this method only works for atoms with a stable negative ion state. Fortunately, most of the elements have such a state, with the notable exceptions of the noble gases and nitrogen (Hotop and Lineberger, 1985). A comprehensive review of theoretical and experimental work on surface ionization has been given by Los and Geerlings (1990).

In the past 20 years, surface ionization has been studied extensively for potential application in fusion plasma research. With this technique, ionization efficiencies[†] of up to 67% in the energy range from several eV to about 1 keV (van Wunnik et al., 1983; Geerlings et al., 1985) have been achieved, using low work function (WF) surfaces for converting neutral particles into negative ions. For plasma measurements on the TORTUR tokamak a neutral particle analyzer using this method has been developed with a detection efficiency[‡] of 5% for 5 eV hydrogen atoms (van Toledo et al., 1992). The application of surface ionization in space research was first

[†]The fraction of ions in the reflected flux
[‡]The ratio of reflected ion flux to the incoming particle flux

proposed by Gruntman (1993b) and Wurz et al. (1993).

Low work function surfaces have been obtained by coating a metallic substrate with a monolayer or less of an alkali metal (Lang, 1971) or an alkaline-earth metal (van Os et al., 1988). The application of this overlayer of metal usually involves a dispenser, which releases defined quantities of the metal upon heating. Since the alkali metal and to a lesser degree the alkaline-earth metal surface are chemically very sensitive, they degrade even in a good vacuum environment after some time, and regeneration of the converter surface at regular intervals is necessary for long-term operation. This regeneration of the converter surface involves heating of the surface to substantial temperatures to evaporate the adsorbates, and the alkali or alkaline-earth metal overlayer. Then, one proceeds with the application of a fresh alkali or alkaline-earth metal layer. In addition to surface heating, the handling of a dispenser introduces some complexity, such as monitoring the WF of the surface (Schletti et al., 2000). Despite these experimental challenges, Cs/W(110) (Aellig et al., 1998) and Ba/W(110) (Schletti, 1996) converter surfaces can in principle be used on a space platform. However, the actual realization of the method using a cesiated tungsten surface was not possible within the framework of a MIDEX mission. For the LENA sensor on IMAGE a highly polished polycrystalline tungsten surface is used for the conversion surface, with the ionization facilitated by natural contaminants, most likely adsorbed water (Moore et al., 2000).

The LENA instrument on the IMAGE mission is the first instrument to use surface ionzation (Moore et al., 2000). A schematic cross section of the instrument in a plane containing the axis of symmetry is shown in Fig. 20 (Ghielmetti et al., 1994; Wurz et al., 1995). The principal elements of the instrument are an entrance collimating system, a conversion unit, an extraction lens, an electrostatic analyzer, and a carbon-foil TOF mass spectrometer with 2-D position sensing. Neutral and charged particles enter the instrument via the external aperture B1 and are collimated in angle and area by the entrance slit S1. An electrostatic deflector removes all incoming ions with energies less than 100 keV, while a broom magnet deflects all electrons with energies below 200 keV. The remaining neutral particles proceed until they strike the conversion surface (C) at a shallow angle, where a considerable fraction of the reflected particles becomes negatively charged. These negative ions are accelerated away from the converter surface and focused by a wide-aperture low-aberration lens (L) in the S2 slit plane. The circular slit, S2, is set to transmit ions with initial energies within a passband of about 10 eV to 1 keV. The transmitted ions are further accelerated to about 20 keV before they enter the electrostatic analyzer (EA), which is configured to be focusing in elevation angle in the image plane of the carbon foil. Upon striking the carbon foil, placed in the focal plane of the EA, the negative ions produce secondary electrons which provide the start pulse as well as the azimuth and radial position information. Particles (ions and neutrals) transmitted through the carbon-foil proceed to the stop MCP.

The entire instrument is rotationally symmetric about a vertical axis co-located with the S1 entrance slit providing a field-of-view in azimuth angle of 90°. Particles that enter the analyzer through the slit S1 maintain their initial velocity direction except for non-specular reflection at the conversion surface. This effect is minimized through special ion optical design of the acceleration lens system and careful selec-

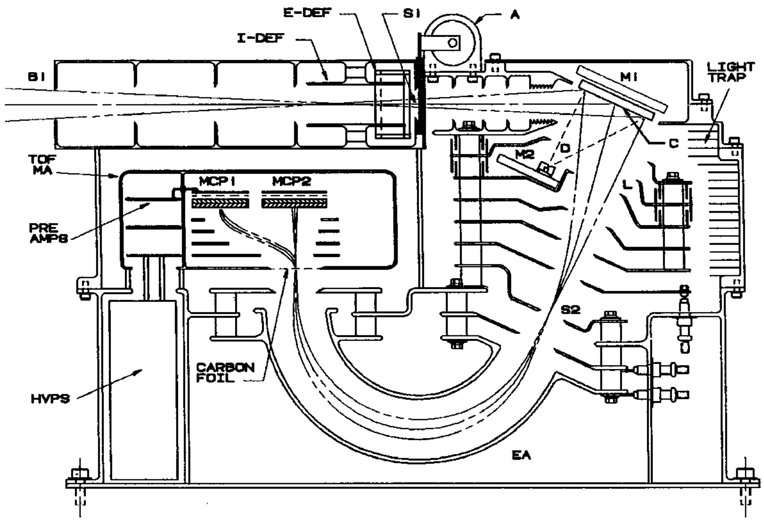

Fig. 20: Schematic drawing of the LENA instrument on the IMAGE mission, showing the principal components. The axis of rotation is perpendicular to the presented view of the instrument. The entrance collimating system defines the elevation angle acceptance through slits B1 and S1 and contains the ion and electron deflectors I-DEF and E-DEF. Other key elements are the conversion surface C, the cesium dispenser D, the secondary electron guiding magnets M1 and M2, extraction lens L, energy limiting slit S2, spherical electrostatic analyzer EA, and the time-of-flight mass analyzer MA (from Wurz et al., 1995).

tion of the converter surface. As a result, a direct correlation between the azimuth direction and the position on the plane of the carbon foil is achieved, which allows the original arrival direction of the neutral atom to be deduced. In a similar manner, energy information is extracted from the radial impact position.

In the next generation of such instruments, converter surfaces will be used where the regeneration of the converter surface would be easier or not necessary at all. Surfaces, which are known to be good secondary electron emitters, are good candidates since the secondary electron emission and the formation of negative ions upon scattering are related processes. Recently, high ionization efficiencies using a polycrystalline diamond surface were found (Wurz et al., 1997). The negative ion fractions in the reflected particle flux were 5.5% and 29% for hydrogen and oxygen, respectively. Diamond, a chemically inert and very stable surface, and a wide bandgap insulator, appears to be a potential candidate for an application on a space platform. Encouraged by our initial results we investigated several different polycrystalline diamond samples produced in different ways. In addition, we studied two monocrystalline natural diamond surfaces of type IIa and IIb with (111) orientation, barium-zirconate ($BaZrO_3$) surfaces, and aluminum-nitride (AlN) surfaces (Jans et al., 2000). All these surfaces are potential candidates for an application on a space platform.

9 Conclusions

We have reviewed all the different methods currently used to detect ENAs or being developed for future use for the detection of energetic neutral atoms. We also discussed some representative examples of instruments. Figure 21 shows the energy range relevant for ENA measurements, ranging from ≈ 10 eV to < 10 MeV. The approximate energy ranges of the different experimental methods are also indicated in Fig. 21. No single method can cover the whole energy range. Moreover, the methods also have different performance in terms of mass-, energy-, time-, and image-resolution, which has to be considered when deciding on the instrumentation for a future mission.

At the highest energies, the HENA energy range, instruments with SSDs have to be used: i.e., the TOF-E and the pinhole camera with a solid state detector. Of course, these methods can be combined in one instrument. These are probably the most advanced instruments for ENA detection, since there is a lot of heritage from energetic ion instrumentation.

The MENA energy range is covered by the pinhole camera with the MCP detector, with an energy range from about 100 eV to several 100 keV. If the pinhole camera is combined with a TOF measurement, the lowest particle energies which can be measured are about 1 keV, because of the thin start-foil the particles have to pass. The surface scattering TOF also operates in the MENA energy range. Since the ENAs don't have to pass through matter, the energy range extends from about 100 eV to about 100 keV. Remember that for both instruments the mass identification relies on the different secondary electron yields for different elements, which is a severe limitation. It is anticipated that with the availability of super-thin SSDs the TOF-E instruments will cover the energy range down to 1 keV as well.

At the lowest ENA energies considered here, the LENA energy range, only surface ionization will give a sufficiently high detection efficiency. Due to the novelty of the technique, the implementation of surface ionization in space instrumentation is not very mature at the moment. It is anticipated that in the future, smaller and lighter designs will be accomplished than was possible for the LENA instrument on the IMAGE mission. The detection method employed in the Ulysses GAS instrument also falls in the LENA range. However, the Ulysses GAS instrument is specially adapted for measurements of the helium component of the interstellar gas. It is difficult to see how this method can be used for other measurements. The foil collection technique is also sensitive in the LENA energy range, and extending to energies even in the HENA range. The foil collection technique is a very mature method, which is reflected in the ambitious scientific goals set for the *Genesis* mission.

ENA detection, and in particlar ENA imaging for remote sensing, is a fast-growing area in space research. It is anticipated that there will be many new ENA imaging instruments on missions to planets and their moons in the near future. Moreover, the research program *Quest 3—How do the Sun and Galaxy Interact?* has highest priority at NASA, since the question of spacecraft propulsion to reach the boundaries of the heliosphere (100 – 200 AU) in a reasonable time (≈ 10 years) seems to be solvable using ion thrusters or solar sails. In particular, the NASA missions *In-*

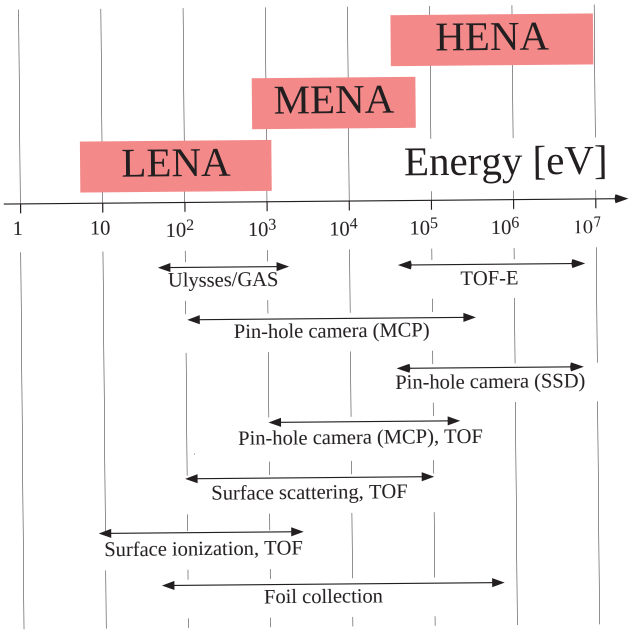

Fig. 21: Energy ranges of the different experimental techniques applicable for the detection of ENAs.

terstellar Probe (projected start in 2007) and *Interstellar Composition Observatory* (possible start in 2020) will carry, among others, ENA imaging instruments to study the composition and the physical parameters of the local interstellar gas. Until the realization of these big missions there will be some smaller missions, e.g., the *Interstellar Gas Sampler*, a NASA mission of the MIDEX class, which will also have instruments for the detection of ENAs.

Acknowledgements. I am grateful to the organizers of the DPG spring school to have been given the opportunity to present this topic. Furthermore, I wish to acknowledge the contributions of F. Bühler, E. Flückiger, and S. Jans, University of Bern, and of R. Müller-Mellin, University of Kiel. This work was supported by the Swiss National Science Foundation.

References

Aellig, M.R., P. Wurz, R. Schletti, P. Bochsler, A.G. Ghielmetti, E.G. Shelley, S.A. Fuselier, J.M. Quinn, F. Herrero, and M.F. Smith, Surface ionization with cesiated converters for space applications, in *Measurement Techniques for Space Plasmas, AGU Monograph*, *103*, 289–295, 1998.

Axford, W.I., F. Bühler, and H.J.A. Chivers, Auroral helium precipitation, *J. Geophys. Res.*, *77(34)*, 6724–6730, 1972.

Bamert, K., Supra-thermal particles in transient solar events, *Master's Thesis*, University of Bern, Switzerland, 1999.

Banks, P.M., Magnetosphere, ionosphere and atmosphere interactions, in *Solar System Plasma Physics*, C.F. Kennel, L.J. Lanzerotti, and E.N. Parker (eds.), North-Holland Publishing Company, *Volume II*, 59–103, 1979.

Barabash, S., O. Norberg, R. Lundin, S. Olsen, K. Lundin, P. Carlson, P. C:son Brandt, E.C. Roelof, C.J. Chase, B.H. Mauk, H. Koskinen, and J. Rynö, Energetic neutral atom imager on the Swedish microsatellite Astrid, in *Measurement Techniques in Space Plasmas*, R.F. Pfaff, J.E. Borovsky, and D.T. Young (eds.), *AGU Monograph*, *103*, 257–262, 1998.

Beauchemin, G., and R. Drouin, Collisional and radiative processes, in *Beam-Foil Spectroscopy*, Plenum Press, New York and London, 687–694, 1975.

Beiersdorfer, P., A.L. Roquemore, and R. Kaita, Characteristics of compact solid-target charge exchange analyzers for energetic ion diagnostics on tokamaks, *Rev. Sci. Instr.*, *58(11)*, 2092–2098, 1987.

Bernstein, W., A.J. Cole, and R.L. Wax, Penetration of 1–20 keV ions through thin carbon foils, *Nucl. Instr. Meth.*, *90*, 325–328, 1970.

Bertollini, G., and A. Coche, *Semiconductor Detectors*, Wiley, New York, 1968.

Betz, G., and K. Wien, Energy and angular distributions of sputtered particles, *Int. J. Mass Spectr.*, *140*, 1–110, 1994.

Brehm, B., J. Grosser, T. Ruscheinski, and M. Zimmer, Absolute detection efficiencies of a microchannel plate detector for ions, *Meas. Sci. Technol.*, *6*, 953–958, 1995.

Bühler, F., P. Eberhardt, J. Geiss, and J. Schwarzmüller, Trapped solar wind helium and neon in Surveyor 3 material, *Earth Plan. Sci. Lett.*, *10*, 297–306, 1971.

Bühler, F., W.I. Axford, H.J.A. Chivers, and K. Marti, Helium isotopes in the aurora, *J. Geophys. Res.*, *81(1)*, 111–115, 1976.

Bühler, F., D.L. Lind, J. Geiss, and O. Eugster, The interstellar gas experiment: Analysis in progress, in *LDEF—69 Months in Space*, *NASA Conf. Pub.*, *3194(2)*, 705–722, 1993.

Bühler, F., private communication, 1999.

Burch, J., Imager for Magnetopause-to-Aurora Global Exploration (IMAGE) *NASA MIDEX program*, Southwest Research Institute, San Antonio, TX, USA, 1995.

Burrows, C.N., A.J. Lieber, and V.T. Zaviantseff, Detection efficiency of a continuous channel electron multiplier for positive ions, *Rev. Sci. Instr.*, *38(10)*, 1477–1481, 1967.

Curtis, C.C., and K.C. Hsieh, Remote sensing of planetary magnetospheres: Imaging via energetic neutral atoms, in *Solar System Plasma Physics*, J.H. Waite Jr., J.L. Burch, and R.L. Moore (eds.), *Geophysical Monograph*, *54*, 247–251, 1989.

Echenique, P.M., R.M. Niemienen, J.C. Ashley, and R.H. Ritchie, Nonlinear stopping power of an electron gas for slow ions, *Phys. Rev. A*, *33(2)*, 897–904, 1986.

Fleischmann, H.H., and R.A. Young, Stripping and ionization in low-energy collisions of H on O_2 and N_2, *Phys. Lett.*, *29A*, 287–288, 1969.

Fraser, G.W., *X-Ray Detectors in Astronomy*, Cambridge University Press, Cambridge, 1989.

Frisch, P.C., and D.G. York, Interstellar clouds near the Sun, in *The Galaxy and the Solar System*, R. Smoluchowski, J.N. Bahcall, and M.S. Matthews (eds.), Tucson, The University of Arizona Press, 83–100, 1986.

Funsten, H.O., D.J. McComas, and M.A. Gruntman, Neutral atom imaging: UV rejection techniques, in *Measurement Techniques in Space Plasmas*, R.F. Pfaff, J.E. Borovsky, and D.T. Young (eds.), *Geophysical Monograph*, *103*, 235–249, 1998.

Geerlings, J.J.C., P.W. van Amersfoort, L.F.T. Kwakman, E.H.A. Granneman, and J. Los, H^- formation in proton-metal collisions, *Surf. Sci.*, *157*, 151–161, 1985.

Geiss, J., P. Eberhardt, F. Bühler, J. Meister, and P. Signer, Apollo 11 and 12 solar wind composition experiments: Fluxes of He and Ne isotopes, *J. Geophys. Res.*, *75(31)*, 5972–5979, 1970.

Geiss, J., F. Bühler, H. Cerruti, P. Eberhardt, and C. Filleux, Solar wind composition experiment, *Apollo 16 Preliminary Science Report*, *NASA SP-315(14)*, 1–10, 1972.

Geiss, J., and M. Witte, Properties of the interstellar gas inside the heliosphere, *Space Sci. Rev.*, *78*, 229–238, 1996.

Ghielmetti, A.G., E.G. Shelley, S. Fuselier, P. Wurz, P. Bochsler, F. Herrero, M.F. Smith, and T. Stephen, Mass spectrograph for imaging low energy neutral atoms, *Opt. Eng.*, *33*, 362–370, 1994.

Gloeckler, G., and K.C. Hsieh, Time-of-flight technique for particle identification at energies from 2 – 400 keV/nucleon, *Nucl. Instr. Meth.*, *165*, 537–544, 1979.

Gruntman, M.A., S. Grzedzielski, and V.B. Leonas, Neutral solar wind experiment, in *Physics of the Outer Heliosphere*, S. Grzedzielski and D.E. Page (eds.), Pergamon Press, New York, 355–358, 1989.

Gruntman, M.A., Coded-aperture technique for magnetospheric imaging: advantages and limitations, *SPIE*, *2008*, 58–73, 1993.

Gruntman, M.A., A new technique for in situ measurement of the composition of neutral gas in interplanetary space, *Planet. Space Sci.*, *41(4)*, 307–319, 1993.

Gruntman, M., Energetic neutral atom imaging of space plasmas, *Rev. Sci. Instrum.*, *68(10)*, 3617–3656, 1997.

Gubler, L., P. Wurz, P. Bochsler, and E. Möbius (1995), High resolution isochronous mass spectrometer for space plasma applications, *Int. J. Mass Spectr.*, *148*, 77–96, 1995.

Hasselkamp, D., Kinetic electron emission from solid surfaces under ion bombardment, in *Particle In-*

duced Electron Emission II, Springer Tracts in Modern Physics, *123*, 1–95, 1991.

Herrero, F.A., and M.F. Smith, Imager for low energy neutral atoms (ILENA): Imaging neutrals from the magnetosphere at energies below 20 keV, *SPIE.*, *1744*, 32–39, 1992.

Hilchenbach, M., K.C. Hsieh, D. Hovestadt, B. Klecker, H. Grünwaldt, P. Bochsler, F.M. Ipavich, A. Bürgi, E. Möbius, F. Gliem, I. Axford, H. Balsiger, W. Bornemann, M.A. Coplan, A.B. Galvin, J. Geiss, G. Gloeckler, S. Hefti, D.L. Judge, R. Kallenbach, P. Laeverenz, M.A. Lee, S. Livi, G.G. Managadze, E. Marsch, M. Neugebauer, H.S. Ogawa, K.-U. Reiche, M. Scholer, M.I. Verigin, B. Wilken, and P. Wurz, Detection of 55–80 keV hydrogen atoms of heliospheric origin by CELIAS/HSTOF on SOHO, *Astrophys. J.*, *503*, 916–922, 1998.

Hilchenbach, M., et al., Heliospheric energetic neutral atoms, this volume, 1999.

Högberg, G., H. Nordén, and H.G. Berry, Angular distribution of ions scattered in thin carbon foils, *Nucl. Instr. Meth.*, *90*, 283–288, 1970.

Hölzl, J., and F.K. Schulte, Work function of metals, *Springer Tracts in Modern Physics*, *85*, 1–150, 1979.

Hotop, H., and W.C. Lineberger, Binding energies in atomic negative ions: II, *J. Phys. Chem. Ref. Data*, *14(3)*, 731–750, 1985.

Hovestadt, D., M. Hilchenbach, A. Bürgi, B. Klecker, P. Laeverenz, M. Scholer, H. Grünwaldt, W.I. Axford, S. Livi, E. Marsch, B. Wilken, P. Winterhoff, F.M. Ipavich, P. Bedini, M.A. Coplan, A.B. Galvin, G. Gloeckler, P. Bochsler, H. Balsiger, J. Fischer, J. Geiss, R. Kallenbach, P. Wurz, K.-U. Reiche, F. Gliem, D.L. Judge, K.H. Hsieh, E. Möbius, M.A. Lee, G.G. Managadze, M.I. Verigin, and M. Neugebauer, CELIAS: The Charge, Element, and Isotope Analysis System for SOHO, *Solar Physics*, *162*, 441–481, 1995.

Hsieh, K.C., E. Keppler, and G. Schmidtke, Extreme ultraviolet induced forward photoemission from thin carbon foils, *J. Appl. Phys.*, *51*, 2242–2246, 1980.

Hsieh, K.C., and C.C. Curtis, Remote sensing of planetary magnetospheres: Mass and energy analysis of energetic neutral atoms, in *Solar System Plasma Physics*, J.H. Waite Jr., J.L. Burch, and R.L. Moore (eds.), *Geophysical Monograph*, *54*, 159–164, 1989.

Hsieh, K.C., B.R. Sandel, V.A. Drake, and R.S. King, H Lyman α transmittance of thin C and Si/C foils for keV particle detectors, *Nucl. Instr. Meth. B*, *61*, 187–193, 1991.

Hsieh, K.C., and C.C. Curtis, Imaging space plasma with energetic neutral atoms without ionization, in *Measurement Techniques in Space Plasmas*, R.F. Pfaff, J.E. Borovsky, and D.T. Young (eds.), *Geophysical Monograph*, *103*, 235–249, 1998.

Ivkova, T.M., V.K. Lichtenstein, E.D. Olshanski, Preparation and application of ultra-thin superstrong diamond-like carbon targets for laboratory and space experiments, *Nucl. Instr. Meth.*, *A 362*, 77–80, 1995.

Jans, S., Definition of the optical components for the NPD sensor on Mars Express, *Master's Thesis*, University of Bern, Switzerland, 1999.

Jans, S., P. Wurz, R. Schletti, T. Fröhlich, E. Hertzberg, and S.A. Fuselier, Negative ion production by surface ionization using aluminium-nitride surfaces, *J. Appl. Phys.*, in press, 2000.

Keath, E.P., G.B. Andrews, A.F. Cheng, S.M. Krimigis, B.H. Mauk, D.G. Mitchell, and D.J. Williams, Instrumentation for energetic neutral atoms imaging of magnetospheres, in *Solar System Plasma Physics*, J.H. Waite Jr., J.L. Burch, and R.L. Moore (eds.), *Geophysical Monograph*, *54*, 165–170, 1989.

Kirsch, E., S.M. Krimigis, W.-H. Ip, and G. Gloeckler, X-ray and energetic particle emission from Saturn's magnetosphere, *Nature*, *292*, 718–721, 1981.

Kirsch, E., S.M. Krimigis, J.W. Kohl, and E.P. Keath, Upper limits for X-ray and energetic particle emission from Jupiter: Voyager 1 results, *J. Geophys. Res.*, *8*, 169–172, 1981.

Knoll, G.F., *Radiation Detection and Measurement*, Wiley, New York, 1989.

Lampton, M., and C.W. Carlson, Low-distortion resistive anode for two-dimensional position-sensitive MCP systems, *Rev. Sci. Instr.*, *50(9)*, 1093–1097, 1979.

Lang, N.D., Theory of work-function changes induced by alkali adsorption, *Phys. Rev.*, *B4*, 4234–4244, 1971.

Lind, D.L., J. Geiss, and W. Stettler, Solar terrestrial noble gases in magnetospheric precipitation, *J. Geophys. Res.*, *84*, 6435–6442, 1979.

Lind, D.L., J. Geiss, F. Bühler, and O. Eugster, The interstellar gas experiment, in *LDEF—69 Months in Space*, A.S. Levine (ed.), *NASA Conf. Pub.*, *3134*, 585–594, 1991.

Los, J., and J.J.C. Geerlings, Charge exchange in atom-surface collisions, *Phys. Reports*, *190(3)*, 133–190, 1990.

Lundin, R., S. Barabash, O. Nordberg, M. Yamauchi, S. Livi, N. Krupp, J. Woch, M. Grande, J.-A. Sauvaud, H. Koskinen, E. Kallio, S. Orsini, R. Cerulli-Irelli, D. Winningham, J. Sharber, R. Frahm, E. Roelof, D. Williams, J. Kozyra, A. Fedorov, J. Luhmann, J.C. Hsieh, B.R. Sandel, and C.C. Curtis, *ASPERA-3: Analyzer of Space Plasmas and Energetic Atoms*, Swedish Institute of Physics, Kiruna, Sweden, 1998.

Mall, U., Fremd Ionen im Sonnenwind, this volume, 1999.

McEntire, R.W., and D.G. Mitchell, Instrumentation for global magnetospheric imaging via energetic neutral atoms, in *Solar System Plasma Physics*, J.H. Waite Jr., J.L. Burch, and R.L. Moore (eds.), *Geophysical Monograph*, *54*, 69–80, 1989.

Meinel, A.B., Doppler-shifted auroral hydrogen emission, *Astrophys. J.*, *113*, 50–54, 1951.

Martin, C., P. Jelinsky, M. Lampton, R.F. Malin, and H.O. Anger, Wedge-and-strip anodes for centroid-finding position-sensitive photon and particle detectors, *Rev. Sci. Instr.*, *52(7)*, 1067–1074, 1981.

Mitchell, D.G., A.F. Cheng, S.M. Krimigis, E.P. Keath, S.E. Jaskulek, B.H. Mauk, R.W. McEntire, E.E. Roelof, D.J. Williams, K.C. Hsieh, and V.A. Drake, INCA: The ion neutral camera for energetic neutral atom imaging of the Saturnian magnetosphere, *Opt. Eng.*, *32*, 3096–3101, 1993.

Mitchell, D.G., S.M. Krimigis, A.F. Cheng, K.C. Hsieh, S.E. Jaskulek, E.P. Keath, B.H. Mauk, R.W. McEntire, E.C. Roelof, C.E. Schlemm, B.E. Tossman, and D.J. Williams, Imaging-neutral camera (INCA) for the NASA Cassini mission to Saturn and Titan, *SPIE Proc.*, *2803*, 154–161, 1996.

Mitchell, D.G., S.E. Jaskulek, C.E. Schlemm, E.P. Keath, R.E. Thompson, B.E. Tossman, J.D. Boldt, J.R. Hayes, G.B. Andrews, N. Paschalidis, D.C. Hamilton, R.A. Lundrgren, E.O. Tums, P. Wilson IV, H.D. Voss, D. Prentice, K.C. Hsieh, C.C. Curtis, and F.R. Powell, High energy neutral atom (HENA) imager for the IMAGE mission, *Space Sci. Rev.*, in press, 2000.

Möbius, E., D. Hovestadt, B. Klecker, M. Scholer, G. Gloeckler, and F.M. Ipavich, Direct observation of He^{+} pick-up ions of interstellar origin in the solar wind, *Nature*, *318*, 426–429, 1985.

Moore, T.E., D. Chornay, M.R. Collier, F.A. Herrero, J. Johnson, M.A. Johnson, J.W. Keller, J.F. Laudadio, J.F. Lobell, K.W. Ogilvie, P. Rozmarynowski, M.F. Smith, S.A. Fuselier, A.G. Ghielmetti, E. Hertzberg, D.C. Hamilton, R. Lundgren, P. Wilson, P. Walpole, T. Stephen, B. VanZyl, P. Wurz, and J. Quinn, The low energy neutral atom imager for the IMAGE mission, *Space Sci. Rev.*, in press, 2000.

Moritz, J., Energetic protons at low altitudes: A newly discovered radiation belt phenomenon and its explanation, *Z. Geophys.*, *38*, 701–717, 1972.

Oberheide, J., P. Wilhelms, and M. Zimmer, New results on the absolute ion detection efficiencies of a microchannel plate, *Meas. Sci. Technol.*, *8*, 351–354, 1997.

Oetliker, M., Response of a passivated implanted planar silicon (PIPS) detector for heavy ions with energies between 25 and 360 keV, *Nucl. Instr. Meth. A*, *337*, 145–148, 1993.

Rairden, R.L., L.A. Frank, and J.D. Craven, Geocoronal imaging with Dynamics Explorer, *Geophys. Res. Lett.*, *10(7)*, 533–536, 1983.

Rairden, R.L., L.A. Frank, and J.D. Craven, Geocoronal imaging with Dynamics Explorer, *J. Geophys. Res.*, *91(A12)*, 13613–13630, 1986.

Roelof, E.C., D.G. Mitchell, and D.J. Williams, Energetic neutral atoms ($E \approx 50$ keV) from the ring current: IMP 7/8 and ISEE-1, *J. Geophys. Res.*, *90*, 10991–11008, 1985.

Roelof, E.C., Energetic neutral atom image of a storm-time ring current, *Geophys. Res. Lett.*, *14*, 652–655, 1987.

Schletti, R., Anwendung der Oberflächenionisation in Raumforschungsexperimenten, *Master's Thesis*, University of Bern, Switzerland, 1996.

Schletti, R., T. Fröhlich, and P. Wurz, Metallic workfunction measurement in the range 2 eV to 3.3 eV using a blue LED source, *Rev. Sci. Instr.*, in press, 2000.

Scime, E.E., H.O. Funsten, D.J. McComas, K.R. Moore, and M.A. Gruntman, Novel low-energy neutral atom imaging technique, *Opt. Eng.*, *33(2)*, 357–361, 1994.

Siegmund, O.H.W., J.M. Stock, D.R. Marsh, M.A. Gummin, R. Raffanti, J. Hull, G.A. Gains, B. Welsh, B. Donakowski, P. Jelinsky, T. Sasseen, and J.L. Tom, Delay line detectors for the UVCS and SUMER instruments on the SOHO satellite, *SPIE*, *2280*, 89–100, 1994.

Smart, D.F., and M.A. Shea, Galactic cosmic radiation and solar energetic particles, in *Handbook of Geophysics and the Space Environment*, Air Force Geophysics Laboratory, chapter 6, 1985.

Spjeldvik, W.N., and P.L. Rothwell, The radiation belts, in *Handbook of Geophysics and the Space Environment*, Air Force Geophysics Laboratory, chapter 5, 1985.

Stix, M., *The Sun*, A&A Library, Springer Verlag, Berlin, 1991.

Timothy, J.G., G.H. Mount, and R.L. Bybee, Multi-anode microchannel arrays, *IEEE Trans. Nucl. Sci.*, *NS-28(1)*, 689–697, 1981.

Tinsley, B.A., Neutral atom precipitation—a review, *J. Atmos. Terr. Phys.*, *43(5/6)*, 617–632, 1981.

Tremsin, A.S., J.F. Pearson, J.E. Lees, and G.W. Fraser, The microsphere plate: a new type of electron multiplier, *Nucl. Instr. Meth.*, *A 368*, 719–730, 1996.

van Os, C.F.A., P.W. Amersfoort, and J. Los, Negative ion formation at a barium surface exposed to an intense positive-hydrogen ion beam, *J. Appl. Phys.*, *64*, 3863–3873, 1988.

van Toledo, W., R. van Buuren, A.J.H. Donné, and H. de Kluiver, H^--conversion aided detection of low-energy H^0 fluxes from the TORTUR tokamak in a time-of-flight analyzer, *Rev. Sci. Instr.*, *63(4)*, 2223–2231, 1992.

van Wunnik, J.N.M., J.J.C. Geerlings, E.H.A. Granneman, and J. Los, The scattering of hydrogen atoms from a cesiated tungsten surface, *Surf. Sci.*, *131*, 17–33, 1983.

Voss, H.D., J. Modilia, H.L. Collin, and W.L. Imhof, Satellite observations and instrumentation for measuring energetic neutral atoms, *Opt. Eng.*, *32(12)*, 3083–3089, 1993.

Wilken, B., I.A. Daglis, A. Milillo, S. Orsini, T. Doke, S. Livi, and S. Ullaland, Energetic neutral atoms in the outer magnetosphere: An upper flux limit obtained with the HEP-LD spectrometer on board GEOTAIL, *Geophys. Res. Lett.*, *24*, 111–114, 1997.

Witte M., H. Rosenbauer, E. Keppler, H. Fahr, P. Hemmerich, H. Lauche, A. Loidl, and R. Zwick, The interstellar neutral-gas experiment on ULYSSES, *Astron. Astrophys. Suppl. Ser.*, *92*, 333–348, 1992.

Witte M., H. Rosenbauer, M. Banaszkiewicz, and H. Fahr, The Ulysses Neutral Gas experiment: Determination of the velocity and temperature of the interstellar neutral helium, *Adv. Space Res.*, *13(6)*, 121–130, 1993.

Witte, M., M. Banaszkiewicz, and H. Rosenbauer, Recent results on the parameters of the interstellar helium from the Ulysses/GAS experiment, *Space Sci. Rev.*, *78*, 289–296, 1996.

Wiza, J.L., Microchannel plate detectors, *Nucl. Instr. Meth.*, 62, 587–601, 1979.

Wurz, P., P. Bochsler, A.G. Ghielmetti, E.G. Shelley, F. Herrero and M.F. Smith, Concept for the HI-LITE neutral atom imaging instrument, in *Proceedings of Symposium on Surface Science*, P. Varga and G. Betz (eds.), Kaprun, Austria, 225–230, 1993.

Wurz, P., M.R. Aellig, P. Bochsler, A.G. Ghielmetti, E.G. Shelley, S.A. Fuselier, F. Herrero, M.F. Smith, and T.S. Stephen, Neutral atom mass spectrograph, *Opt. Eng.*, *34*, 2365–2376, 1995.

Wurz, P., R. Schletti and M.R. Aellig, Hydrogen and oxygen negative ion production by surface ionization using diamond surfaces, *Surf. Sci.*, *373*, 56–66, 1997.

Wurz, P., L. Gubler, P. Bochsler, and E. Möbius, Isochronous mass spectrometer for space plasma applications, in *Measurement Techniques in Space Plasmas*, R.F. Pfaff, J.E. Borovsky, and D.T. Young (eds.), *AGU Monograph*, *102*, 229–235, 1998.

Wurz, P., Heavy ions in the solar wind: Results from SOHO/CELIAS/MTOF, *Habilitation Thesis*, University of Bern, Switzerland, 1999.

Yermolaev, Yu.I, Large-scale structure of the solar wind and its relationship with solar corona: *PROGNOZ* 7 observations, *Planet. Space Sci.*, *39(10)*, 1351–1361, 1991.